Journal of Computational Physics 228 (2009) 8053–8084

Contents lists available at ScienceDirect

Journal of Computational Physics

journal homepage: www.elsevier.com/locate/jcp

Construction of explicit and implicit dynamic finite difference schemes and application to the large-eddy simulation of the Taylor–Green vortex

Dieter Fauconnier *, Chris De Langhe, Erik Dick

Department of Flow, Heat and Combustion Mechanics, Ghent University, St. Pietersnieuwstraat 41, B-9000 Ghent, Belgium

ARTICLE INFO

Article history:
Received 9 March 2009
Received in revised form 22 July 2009
Accepted 24 July 2009
Available online 3 August 2009

Keywords:
Dynamic finite difference schemes
Dispersion-Relation Preserving schemes
Large-eddy simulation
Richardson Extrapolation
Taylor–Green vortex

ABSTRACT

A general class of explicit and implicit *dynamic* finite difference schemes for large-eddy simulation is constructed, by combining Taylor series expansions on two different grid resolutions. After calibration for $\mathrm{Re} \to \infty$, the dynamic finite difference schemes allow to minimize the dispersion errors during the calculation through the real-time adaption of a dynamic coefficient. In case of DNS resolution, these dynamic schemes reduce to Taylor-based finite difference schemes with formal asymptotic order of accuracy, whereas for LES resolution, the schemes adapt to Dispersion-Relation Preserving schemes. Both the explicit and implicit dynamic finite difference schemes are tested for the large-eddy simulation of the Taylor–Green vortex flow and numerical errors are investigated as well as their interaction with the dynamic Smagorinsky model and the multiscale Smagorinsky model. Very good results are obtained.

1. Introduction

Direct numerical simulation of turbulent flows implies that all scales of motion must be resolved accurately in order to predict well the evolution of the flow. This approach, however, is known to be prohibitively expensive in case of high-Reynolds numbers, due to excessive grid requirements to resolve the finest vortex structures in the turbulent flow. Almost since the early days of Computational Fluid Dynamics, various approaches and strategies have therefore been developed to overcome these excessive grid requirements. In particular, large-eddy simulation (LES) is evolving in recent years into a mature simulation technique for turbulent flows, with the potential to combine cost effectiveness with accuracy [1]. The classic philosophy behind large-eddy simulation is to resolve only the largest, unsteady and flow specific, turbulent motions, which are part of the energy containing range or the inertial subrange. Since the important main features of the flow are resolved, the LES solution is believed to provide a statistically accurate prediction of the mean flow.

In recent years, the necessity for numerical quality in DNS and especially LES of turbulent flows, has been investigated by several researchers [2–5]. Aside from aliasing errors, which should be prevented by filtering out all scales of motion beyond the filter cutoff wavenumber $\kappa_c = \frac{2}{3}\kappa_{max}$ [6], discretization errors are mainly responsible for the loss of numerical accuracy in large-eddy simulations. Indeed, although standard finite difference methods or finite volume methods accurately resolve the largest scales of motion on the computational grid ($\kappa \ll \kappa_{max}$), the numerical accuracy with which the smallest scales of motion on the computational grid ($\kappa \approx \kappa_{max}$) are resolved is often insufficient. Since these smallest resolved scales typically contain a significant amount of energy in large-eddy simulations, their influence on the evolution of the largest resolved scales and on the mean flow statistics is expected to be significant. Ghosal [2] and Chow and Moin [4] demonstrated that the

DOI of original article: 10.1016/j.jcp.2008.11.014
* Corresponding author. Tel.: +32 9 264 95 21; fax: +32 9 264 35 86.
E-mail address: dieter.fauconnier@ugent.be (D. Fauconnier).

0021-9991/$ - see front matter © 2009 Elsevier Inc. All rights reserved.
doi:10.1016/j.jcp.2009.07.028

standard 2nd-order central finite difference method can lead to large numerical errors which dominate the accuracy of the large-eddy simulation. Therefore, these authors recommend a filter-to-grid cutoff-ratio $\frac{\kappa_c}{\kappa_{max}} \leqslant \frac{1}{4}$ when using a 2nd-order central scheme, to ensure that the magnitudes of the discretization errors remain smaller than the magnitude of the modeled force of the subgrid scales. Although Park and Mahesh [7] found, in an Eddy-Damped Quasi-Normal Markovian (EDQNM) LES of isotropic turbulence, that in case of the 2nd-order scheme, the subgrid force remains dominant at *low* Reynolds numbers, the recommendations of Ghosal [2] and Chow and Moin [4] were confirmed by Berland et al. [5], using EDQNM theory for LES at *high* Reynolds numbers. However, in order to reduce computational costs, it is highly desirable in large-eddy simulation to resolve as much scales of motion as possible on the computational grid. Therefore, the accuracy of the discretization schemes should ideally be guaranteed for all scales up to the dealiasing limit $\kappa_c = \frac{2}{3}\kappa_{max}$. Moreover, since accurate resolution of the smallest scales (characterized by κ_c) increases the required number of nodes with a factor $\left(\frac{2\kappa_{max}}{3\kappa_c}\right)^3$ over those theoretically necessary, small values of $\frac{\kappa_c}{\kappa_{max}}$ are prohibitively expensive for most 3D LES computations.

Although it is common practice in Computational Fluid Dynamics to use (high-order) central schemes based on a truncated Taylor series, leading to a certain formal asymptotic order of accuracy for the largest scales, this is not necessarily the optimal strategy for large-eddy simulation. Indeed, higher-order discretizations are often applied to allow for larger filter-to-grid cut-off-ratios. However in order to obtain acceptable dispersion errors up to $\kappa_c = \frac{2}{3}\kappa_{max}$, which is the maximum resolution on the computational grid, at least the standard 10th-order central scheme or the 6th-order compact Padé scheme are required, which again inevitably leads to increased complexity and/or computational costs. Preserving the global dispersion relation for the full range of scales up to $\kappa_c = \frac{2}{3}\kappa_{max}$ instead of focusing on asymptotic order of convergence, is therefore much more advantageous for large-eddy simulation of turbulent flows. Indeed, it is desirable for LES to have optimized finite difference approximations of the derivatives with similar Fourier characteristics as the analytical derivatives. Although such Dispersion-Relation Preserving (DRP) numerical methods are common in the field of computational aero-acoustics [8–12], where accurate simulation of propagating waves requires highly non-dispersive and non-dissipative finite difference schemes, these techniques are not very common yet in the field of LES and only few authors have applied such methods [12,5].

Recently, Fauconnier et al. [13] successfully developed a new family of *dynamic* finite difference schemes for large-eddy simulation. This class of explicit schemes was constructed by combining Taylor series expansions on two different grid resolutions, which is reminiscent to Richardson Extrapolation. In contrast to Richardson Extrapolation, however, the resulting schemes are not characterized by higher order asymptotic convergence, but rather tend to preserve the global dispersion relation for the full range of scales up to $\kappa_c = \frac{2}{3}\kappa_{max}$. Moreover, in addition to the Dispersion-Relation Preserving schemes of, e.g. [8], these dynamic schemes are optimized dynamically during the simulation according to the instantaneous properties of the flow and dispersion errors are minimized through the real-time adaption of certain coefficients. In case of DNS resolution, i.e. for sufficiently smooth and regular physics on the grid, the dynamic schemes reduce to the standard Taylor-based finite difference schemes with formal asymptotic order of accuracy. However, when going to LES resolution, the schemes adapt in real time to preserve the global dispersion relation. Good properties were shown for the large-eddy simulation of Burgers' equation.

In the present work, a general class of implicit *dynamic* finite difference schemes for large-eddy simulation is constructed, for which the explicit schemes in [13] form a subclass. After introducing the necessary mathematical discretization formalisms, the general class of implicit dynamic finite difference approximations is derived. These schemes are analyzed in Fourier space and the remaining blending factor f in the dynamic schemes is then calibrated to obtain optimal accuracy for $\mathrm{Re} \to \infty$, using a simplified model for the turbulent energy spectrum. Further, the performance of a 2nd- and 4th-order explicit dynamic scheme and a 4th-order implicit dynamic scheme are evaluated for the large-eddy simulation of the three-dimensional Taylor–Green vortex flow, which may be considered as a prototype system for transition into turbulence [14,6]. Two different subgrid models are applied for the LES, i.e. the dynamic Smagorinsky model and the small–small multiscale Smagorinsky model. The total simulation error is then decomposed in order to separate the pure finite difference errors from the modeling errors [15,16]. The numerical accuracy of the developed explicit and implicit dynamic schemes is discussed as well as the sensitivity to the predefined blending factor f and their ability to adjust for anisotropy. Finally, the numerical errors and the modeling errors are compared and their interactions are investigated.

2. Mathematical formalism

Assume a vector field $\mathbf{u}(\mathbf{x}, t)$ defined in continuum space $\mathbb{R}^q$, $q \in \{1, 2, 3\}$. To avoid an overload in notation, we restrict the formulas to one spatial dimension $q = 1$, without loss of generality and we do not write explicitly the dimension in time, such that $u(x, t) = u(x), x \in \mathbb{R}$. Consider further a one-dimensional uniform node distribution with equispaced Cartesian coordinates $x_i \in \mathbb{R}$, $i \in \mathbb{N}$ and spacing $\Delta = x_{i+1} - x_i = x_i - x_{i-1}$. The *explicit* definition of the analytical nth partial derivative of the *continuous* field $u(x)$, $x \in \mathbb{R}$, evaluated in a node x_i, can be written as

$$\frac{\partial^n u}{\partial x^n}(x_i) = \lim_{\Delta \to \epsilon}\left[\frac{1}{\Delta^n}\sum_{j=-r}^{r}\beta_j u(x_{i+j})\right], \quad \epsilon = 0, \tag{1}$$

where β_j denotes a set of weighting coefficients and $2r$ is the number of neighbouring nodes involved in the specific definition. The *stencil width* of the scheme's definition is thus $2r + 1$. Since (1) cannot be satisfied in discrete space, where

inevitably $\epsilon > 0$, the derivative can only have a discrete approximation constructed from a Taylor series expansion. Assuming $u(x)$ an *infinitely differentiable* function, and using the notation $\bar{u}$ for the discrete field and δ for the discrete difference operator, Taylor series expansion for the nth derivative in a node $x = x_i$ can be written as[1]

$$\overline{\frac{\partial^n u}{\partial x^n}}(x_i) = \frac{\delta^n \bar{u}}{\delta x^n}(x_i) + \sum_{k'=k}^{\infty} c^*_{k',n} \Delta^{k'} \overline{\frac{\partial^{k'+n} u}{\partial x^{k'+n}}}(x_i), \tag{3}$$

where the *finite difference approximation* of the partial derivative is defined as

$$\frac{\delta^n \bar{u}}{\delta x^n}(x_i) = \frac{1}{\Delta^n} \sum_{j=-r}^{r} \beta_j \bar{u}(x_{i+j}), \tag{4}$$

and the series' initial index is determined by

$$k = \begin{cases} 2r + 1 - n & \forall n \in 2\mathbb{N} + 1, \\ 2r + 2 - n & \forall n \in 2\mathbb{N}. \end{cases} \tag{5}$$

The remaining series expansion in (3), called the *truncation error*, is convergent and vanishes when $\Delta \to 0$, whereas the first term of the truncation error is the *leading order truncation term*. The finite difference approximation (4) is said to have a formal *order of accuracy k*, denoted as $\mathcal{O}(\Delta^k)$. In 1991, Lele [17] introduced the *implicit* or *Padé* finite difference approximations with compact stencil support by combining expression (3) in node $x = x_i$ with the corresponding expressions in the neighbouring nodes $x = x_{i+l}$, $l \in \mathbb{N}$. The Taylor series expansion for the *implicit* finite difference approximation for the nth derivative is then given by[2]

$$\sum_{l=-q}^{q} \alpha_l \overline{\frac{\partial^n u}{\partial x^n}}(x_{i+l}) = \sum_{j=-r}^{r} \frac{\beta_j}{\Delta^n} \bar{u}(x_{i+j}) + \sum_{k'=k}^{\infty} c^*_{k',n} \Delta^{k'} \overline{\frac{\partial^{k'+n} u}{\partial x^{k'+n}}}(x_i), \tag{7}$$

where the order of accuracy k is given by

$$k = \begin{cases} 2r + 2q + 1 - n & \forall n \in 2\mathbb{N} + 1, \\ 2r + 2q + 2 - n & \forall n \in 2\mathbb{N}. \end{cases} \tag{8}$$

It is obvious that the explicit finite difference approximations (3) can be seen as a subclass of the implicit finite difference approximations (7). Hence, in this work, expression (7) will be used to derive the dynamic finite difference schemes in analogy with [13]. Since DNS and LES are sensitive to numerical dissipation, which can excessively damp small scales, only central schemes will be considered, having a (anti)symmetric set of coefficients β_j and α_l. Although these central schemes are non-dissipative, they can induce dispersion errors, affecting the phase speed of the separate wave components and redistributing energy. For regular fields, which are sufficiently smooth on the computational grid, the Taylor series converges rapidly due to small contributions of the higher derivatives. Hence, the dispersion errors remain low. However, in case of highly fluctuating fields with marginal resolution on the grid, the contributions of the higher derivatives in the truncation terms of the Taylor series become much more important, slowing down the convergence of the Taylor series and thus leading to significant dispersion errors. Standard Taylor-based asymptotic finite difference approximations assume smooth fields and fast convergence of the Taylor series. However, in case of irregular LES-fields, where the Taylor series converges more slowly, it would be much more advantageous to minimize contributions of all terms in the Taylor series to obtain good overall performance. In other words, the best strategy for approximating the derivatives with finite difference techniques depends on the resolution efficiency of the computational grid.

In Fauconnier et al. [13], we developed a class of highly accurate explicit dynamic finite difference schemes which have the ability to adapt to the instantaneous resolution efficiency on the computational grid. It was shown both analytically and numerically that these dynamic finite difference schemes, which were constructed by comparing Taylor series on two different grid resolutions, succeeded in minimizing the dispersion errors during the calculation by minimizing the magnitude of all contributions in the truncation term. In the following, we expand the technique to a general class of implicit finite difference approximations, of which the explicit schemes are a subclass.

[1] The truncation series coefficients $c^*_{k',n}$ are determined as

$$c^*_{k',n} = -\sum_{j=-r}^{r} \frac{\beta_j j^{k'+n}}{(k'+n)!}. \tag{2}$$

[2] The truncation series coefficients $c^*_{k',n}$ are determined as

$$c^*_{k',n} = \sum_{l=-q}^{q} \frac{\alpha_l l^{k'}}{(k')!} - \sum_{j=-r}^{r} \frac{\beta_j j^{k'+n}}{(k'+n)!}. \tag{6}$$

3. A general class of implicit dynamic finite difference approximations

3.1. Introduction

For the construction of the implicit finite difference approximations, the same methodology is adopted as for the construction of the explicit dynamic finite difference approximations in [13]. Consider the Taylor series (7) of the kth-order implicit *central* finite difference approximation for the nth derivative of the continuous and infinitely differentiable field $u(x)$, $x \in \mathbb{R}$, in a node $x = x_i$. Consider further a similar kth-order implicit finite difference approximation for the nth partial derivative on the *same* computational grid with grid spacing Δ, but expressed as if the grid resolution were $\alpha\Delta$, $\alpha \in \mathbb{N}$ such that the stencil width for the explicit part is $2\alpha r + 1$ whereas that for the implicit part is $2\alpha q + 1$. The Taylor series expansion then reads

$$\sum_{l=-q}^{q} \alpha_l \overline{\frac{\partial^n u}{\partial x^n}}(x_{i+\alpha l}) = \sum_{j=-r}^{r} \frac{\beta_j}{(\alpha\Delta)^n} \bar{u}(x_{i+\alpha j}) + \sum_{k'=k}^{\infty} c^*_{k',n} (\alpha\Delta)^{k'} \overline{\frac{\partial^{k'+n} u}{\partial x^{k'+n}}}(x_i). \tag{9}$$

Instead of constructing immediately higher-order approximations, two alternative approaches can be used for achieving higher-order approximations from these series. One can either find a finite difference approximation for the leading order truncation term, or one can eliminate the coefficient of the leading order truncation term by combining the $\mathcal{O}(\Delta^{k+2})$-truncated Taylor series in expressions (7) and (9). The latter technique, known as Richardson Extrapolation, has no direct advantage over the first one, since both lead to a finite difference approximation of formal order of accuracy $k+2$. However, the combination of both techniques can lead to a non-trivial self-adaptive dynamic scheme with basic order of accuracy k, but with better spectral characteristics.

Discretization of the leading order truncation term in both Taylor expansions (7) and (9) with a 2nd-*order* accurate finite difference approximation[3] results into the Taylor series expansions

$$\sum_{l=-q}^{q} \alpha_l \overline{\frac{\partial^n u}{\partial x^n}}(x_{i+l}) = \sum_{j=-r}^{r} \frac{\beta_j}{\Delta^n} \bar{u}(x_{i+j}) + c^*_{k,n} \Delta^k \frac{\delta^{k+n} \bar{u}}{\delta x^{k+n}}\bigg|^{\Delta} + \mathcal{O}(\Delta^{k+2}), \tag{10}$$

$$\sum_{l=-q}^{q} \alpha_l \overline{\frac{\partial^n u}{\partial x^n}}(x_{i+\alpha l}) = \sum_{j=-r}^{r} \frac{\beta_j}{(\alpha\Delta)^n} \bar{u}(x_{i+\alpha j}) + c^*_{k,n} (\alpha\Delta)^k \frac{\delta^{k+n} \bar{u}}{\delta x^{k+n}}\bigg|^{\alpha\Delta} + \mathcal{O}((\alpha\Delta)^{k+2}). \tag{11}$$

Although the theoretical value of the coefficient of the leading order truncation term $c^*_{k,n}$ is known a priori from the Taylor series, it is also possible to determine its value by combining the truncated expressions (10) and (11). The coefficient, obtained in that way, will not necessarily have the same value as the one obtained from the Taylor series, i.e. $c^*_{k,n}$, as it will be a function of $\bar{u}(x)$ and its derivatives. Moreover, it will be shown that the obtained value of the coefficient can be optimal with respect to $\bar{u}(x)$, such that deficiencies of the resulting finite difference approximation, e.g. dispersion errors are minimized.

3.2. Multi-resolution premiss

Fig. 1(left) gives an illustration of the normalized truncation errors $\mathcal{O}(\Delta^{k+2})$ and $\mathcal{O}((\alpha\Delta)^{k+2})$ of the finite difference approximations (10) and (11) as function of the relative wavenumber κ/κ_{max}. Assume that the discrete field $\bar{u}(x)$ is characterized by a cutoff wavenumber κ_c, such that the spectral content relative to the computational grid is limited to the range $[0, \kappa_c/\kappa_{max}]$. The global magnitudes of the truncation errors in Eqs. (10) and (11) are then represented by the area under the curves $\mathcal{O}(\Delta^{k+2})$ and $\mathcal{O}((\alpha\Delta)^{k+2})$. The global difference between the truncation errors in (10) and (11) is indicated by the light-grey area between the curves. Fig. 1 (right) shows the normalized truncation errors $\mathcal{O}(\Delta^k)$ and $\mathcal{O}((\alpha\Delta)^k)$ of the finite difference approximations (10) and (11) where the error is minimized over the wavenumber range $[0, \kappa_c/\kappa_{max}]$, by replacing in each equation $c^*_{k,n}$ with an optimal coefficient $c_{k,n}$. The order of accuracy remains $\mathcal{O}(\Delta^k)$, unless $c_{k,n}$ has the exact Taylor value $c^*_{k,n}$. This follows readily from the expression of the truncation series, given by

$$\mathcal{O}(\Delta^k) = \sum_{k'=k}^{\infty} c^*_{k',n} \Delta^{k'} \overline{\frac{\partial^{k'+n} u}{\partial x^{k'+n}}} - c_{k,n} \Delta^k \left\{ \overline{\frac{\partial^{k+n} u}{\partial x^{k+n}}} - \sum_{k'=2}^{\infty} c^*_{k',k+n} \Delta^{k'} \overline{\frac{\partial^{k'+k+n} u}{\partial x^{k'+k+n}}} \right\}, \tag{12}$$

$$\mathcal{O}((\alpha\Delta)^k) = \sum_{k'=k}^{\infty} c^*_{k',n} (\alpha\Delta)^{k'} \overline{\frac{\partial^{k'+n} u}{\partial x^{k'+n}}} - c_{k,n} (\alpha\Delta)^k \left\{ \overline{\frac{\partial^{k+n} u}{\partial x^{k+n}}} - \sum_{k'=2}^{\infty} c^*_{k',k+n} (\alpha\Delta)^{k'} \overline{\frac{\partial^{k'+k+n} u}{\partial x^{k'+k+n}}} \right\}. \tag{13}$$

[3] Although higher-order discretizations could be perfectly adopted, there would be no advantage in such an approach. Indeed, the higher-order accuracy is entirely determined by the Taylor series in expressions (7) and (9) and not by the accuracy of the discretization of the leading order truncation term. Hence, in this work the 2nd-order approximations are preferred for the discretization of the leading order truncation terms, which is the minimal order of accuracy.

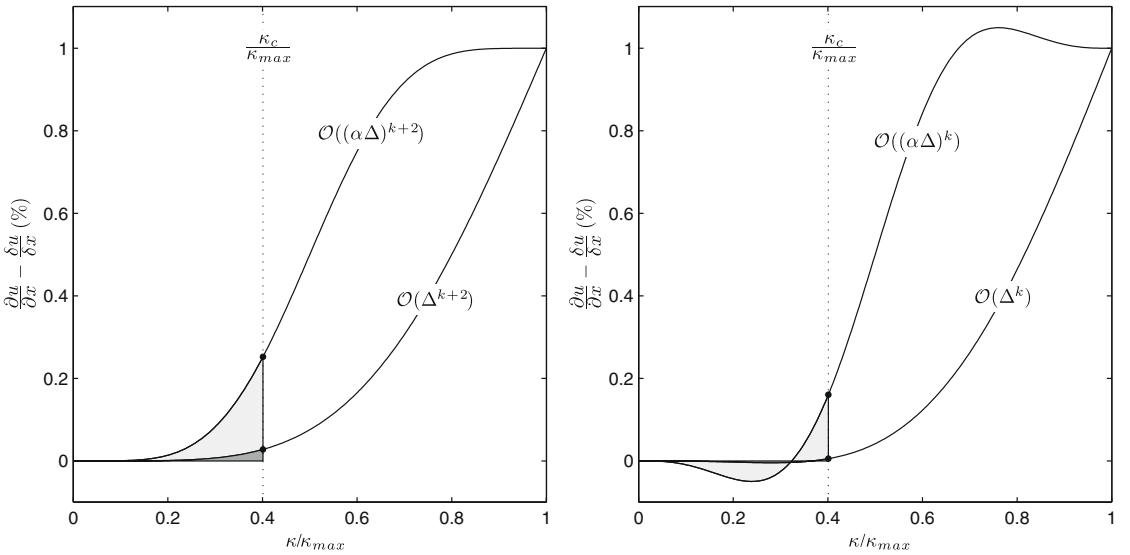

Fig. 1. Multi-resolution premiss. Illustration of the error of a standard finite difference approximation on two different grid resolutions (left) and an optimized finite difference approximation on two different resolutions (right). The global magnitude of the discretization error $\mathcal{O}(\Delta^k)$ is indicated in dark grey, whereas the global difference between $\mathcal{O}(\Delta^k)$ and $\mathcal{O}((\alpha\Delta)^k)$ is indicated in light grey.

Hence, the choice of an optimal $c_{k,n}$ allows to minimize the magnitude of the truncation errors (12) and (13) over the interval $[0, \kappa_c/\kappa_{max}]$, which is more advantageous than increasing the order of accuracy [8–12,5,13].

It was shown in [13] that the optimal coefficient $c_{k,n}$ can be determined by minimizing the difference between the truncated equations (10) and (11), which is equivalent with minimizing the difference between truncation errors (12) and (13). This strategy relies on the assumption of two specific premisses.

1. First, it is postulated that if the magnitudes of both truncation errors (12) and (13) are minimal in the wavenumber range $[0, \kappa_c/\kappa_{max}]$, then, their difference should also be minimal in that range. This is illustrated in Fig. 1 (right). Hence, extracting an optimal value of $c_{k,n}$ from Eqs. (10) and (11) in such a way that the difference between the global magnitudes of the truncation errors (12) and (13) is minimized, should be a sufficient condition for minimizing the global magnitudes of both truncation errors.
2. A necessary condition for the first premiss to be valid is that the role of $c_{k,n}$ must be identical in both Eqs. (10) and (11), which is not necessarily true. Indeed, the optimal value of $c_{k,n}$ depends on the spectral content of the field $\bar{u}(x)$ proportional to the grid resolution, i.e. κ_c/κ_{max}. However, it can be understood that the optimal $c_{k,n}$ for which the truncation error (12) on the fine resolution is minimal does not automatically lead to a minimal truncation error (13) on the coarse resolution and vice versa, unless $\kappa_c/\kappa_{max} = 0$ and thus $c_{k,n} = c^*_{k,n}$ for both resolutions. In order to remedy this inconsistency, it was proposed in [13] to introduce a blending factor f in the coarse resolution equation (11).

3.3. Construction

The construction of the dynamic finite difference schemes is proceeded by replacing the theoretical Taylor coefficient $c^*_{k,n}$ in Eqs. (10) and (11) by the coefficient $c_{k,n}$. Further, a blending factor f is introduced into the coarse resolution equation (11), leading to a modified expression for the discretized leading order truncation term. The resulting equations then yield

$$\sum_{l=-q}^{q} \alpha_l \overline{\frac{\partial^n u}{\partial x^n}}(x_{i+l}) = \sum_{j=-r}^{r} \frac{\beta_j}{\Delta^n} \bar{u}(x_{i+j}) + c_{k,n}\Delta^k \frac{\delta^{k+n}\bar{u}}{\delta x^{k+n}}\bigg|^{\Delta} + \mathcal{O}(\Delta^k), \tag{14}$$

$$\sum_{l=-q}^{q} \alpha_l \overline{\frac{\partial^n u}{\partial x^n}}(x_{i+\alpha l}) = \sum_{j=-r}^{r} \frac{\beta_j}{(\alpha\Delta)^n} \bar{u}(x_{i+\alpha j}) + c_{k,n}(\alpha\Delta)^k \left\{ f \frac{\delta^{k+n}\bar{u}}{\delta x^{k+n}}\bigg|^{\alpha\Delta} + (1-f)\frac{\delta^{k+n}\bar{u}}{\delta x^{k+n}}\bigg|^{\Delta} \right\} + \mathcal{O}((\alpha\Delta)^k). \tag{15}$$

The precise role of f will be clarified in Section 3.6 and a proper value will be determined in Section 4.2. Unless $c_{k,n}$ has the exact Taylor value $c^*_{k,n}$, the order of accuracy in both expressions remains $\mathcal{O}(\Delta^k)$. This is explained by the specific formulation of the truncation error. Subtracting (14) and (15) leads to an expression for the difference between both approximations, i.e.

$$\mathcal{E} = \mathcal{L} + c_{k,n}\mathcal{M} = \mathcal{O}((\alpha\Delta)^k) - \mathcal{O}(\Delta^k) \tag{16}$$

in which

$$\mathcal{L} = -\sum_{l=-q}^{q}\left\{\alpha_l\overline{\frac{\partial^n u}{\partial x^n}}(x_{i+l}) - \alpha_l\overline{\frac{\partial^n u}{\partial x^n}}(x_{i+\alpha l})\right\} + \sum_{j=-r}^{r}\left\{\frac{\beta_j}{\Delta^n}\bar{u}(x_{i+j}) - \frac{\beta_j}{(\alpha\Delta)^n}\bar{u}(x_{i+\alpha j})\right\}, \tag{17}$$

$$\mathcal{M} = (1-\alpha^k)\Delta^k\left|\frac{\delta^{k+n}\bar{u}}{\delta x^{k+n}}\right|^{\Delta} - \alpha^k\Delta^k f\left(\left|\frac{\delta^{k+n}\bar{u}}{\delta x^{k+n}}\right|^{\alpha\Delta} - \left|\frac{\delta^{k+n}\bar{u}}{\delta x^{k+n}}\right|^{\Delta}\right). \tag{18}$$

Following the first premiss, the magnitude of the difference (16), which is a function of the parameter $c_{k,n}$, provides an indication about the accuracy with which the finite difference scheme on the fine grid resolution approximates the analytical derivative (Fig. 1). If the difference is small, the resolution is sufficiently fine in order to ensure an accurate finite difference approximation. In contrast, a large difference $\mathcal{E}$ indicates that the resolution is not fine enough to guarantee an acceptable accuracy of the finite difference approximation. Moreover, an optimal coefficient $c_{k,n}$ can be determined such that the difference $\mathcal{E}$ and the truncation errors on both resolutions are minimized. Hereafter, the cases $f = 0$ and $f \neq 0$ are further investigated.

3.4. Asymptotic high-order schemes for $f = 0$

Consider a blending factor $f = 0$ and assume that the coefficient $c_{k,n} = c^*_{k,n}$. Then, Eqs. (14) and (15) reduce to expressions (10) and (11). Subtracting both equations, as in expression (16), directly results into relation

$$c^*_{k,n}(1-\alpha^k)\Delta^k\left|\frac{\delta^{k+n}\bar{u}}{\delta x^{k+n}}\right|^{\Delta} = \sum_{l=-q}^{q}\alpha_l\left\{\overline{\frac{\partial^n u}{\partial x^n}}(x_{i+l}) - \overline{\frac{\partial^n u}{\partial x^n}}(x_{i+\alpha l})\right\} - \sum_{j=-r}^{r}\frac{\beta_j}{\Delta^n}\left\{\bar{u}(x_{i+j}) - \frac{1}{\alpha^n}\bar{u}(x_{i+\alpha j})\right\} + \mathcal{O}(\Delta^{k+2}). \tag{19}$$

Substitution of this into (10), leads to the finite difference approximation

$$\sum_{l=-q}^{q}\alpha_l\left\{\alpha^k\overline{\frac{\partial^n u}{\partial x^n}}(x_{i+l}) - \overline{\frac{\partial^n u}{\partial x^n}}(x_{i+\alpha l})\right\} = \sum_{j=-r}^{r}\frac{\beta_j}{\Delta^n}\left\{\alpha^k\bar{u}(x_{i+j}) - \frac{1}{\alpha^n}\bar{u}(x_{i+\alpha j})\right\} + \mathcal{O}(\Delta^{k+2}), \tag{20}$$

which is Richardson's Extrapolation formula for Padé schemes. Expression (20) is an approximation with formal asymptotic order of accuracy $\mathcal{O}(\Delta^{k+2})$. Remark that for $f = 0$, the previous procedure applied to (14) and (15) also leads to Richardson's Extrapolation formula (20), regardless the value of the coefficient $c_{k,n}$. In other words, putting $f = 0$ and substituting the value of $c_{k,n}$, determined by relation (16), into Eq. (14) always results into an approximation with formal asymptotic order of accuracy $\mathcal{O}(\Delta^{k+2})$.

Approximation (20) is *incompact* since it involves $2\alpha q + 2\alpha r + 2$ nodes, whereas in principle only $2q + 2r + 4$ nodes are required in order to obtain the same accuracy. Therefore, relation (19) will be enforced in this work in order to guarantee the compactness of the finite difference stencil. Since the aim is to construct optimized finite difference schemes with good Fourier characteristics, abandoning the concept of formal asymptotic order of accuracy, the case where f is different from zero is further investigated.

3.5. Optimized schemes for $f \neq 0$

For the case $f \neq 0$, a more general approach is followed similarly to [13]. The coefficient $c_{k,n}$ is extracted from Eqs. (14) and (15) by means of a least square optimization, in which the least square averaging domain is again an additional degree of freedom. Since the right-hand side in expression (17) does not necessarily have a *compact* stencil, it is first substituted by relation (19). Similarly, the last term in Eq. (18), which is generally *incompact*, can be replaced with a relation that is analogous to relation (19), namely

$$\left|\frac{\delta^{k+n}\bar{u}}{\delta x^{k+n}}\right|^{\alpha\Delta} - \left|\frac{\delta^{k+n}\bar{u}}{\delta x^{k+n}}\right|^{\Delta} \approx c^*_{2,k+n}(1-\alpha^2)\Delta^2\left|\frac{\delta^{k+n+2}\bar{u}}{\delta x^{k+n+2}}\right|^{\Delta}, \tag{21}$$

in which $c^*_{2,k+n}$ is again a constant coefficient known from Taylor series expansion. Substitution of relations (19) and (21) into (17) and (18) yields

$$\mathcal{L} = c^*_{k,n}(\alpha^k - 1)\Delta^k\left|\frac{\delta^{k+n}\bar{u}}{\delta x^{k+n}}\right|^{\Delta}, \tag{22}$$

$$\mathcal{M} = (1-\alpha^k)\Delta^k\left|\frac{\delta^{k+n}\bar{u}}{\delta x^{k+n}}\right|^{\Delta} - \alpha^k\Delta^k f\left\{c^*_{2,k+n}(1-\alpha^2)\Delta^2\left|\frac{\delta^{k+n+2}\bar{u}}{\delta x^{k+n+2}}\right|^{\Delta}\right\}. \tag{23}$$

The optimized *dynamic coefficient* can then be extracted by least square minimization of the difference (16)

$$\frac{\partial}{\partial c_{k,n}}\langle\mathcal{E}^2\rangle = 0, \tag{24}$$

where $\langle\cdot\rangle$ denotes an averaging operator, resulting finally in the *dynamic coefficient*

$$c_{k,n}^{dyn} = -\frac{\langle \mathcal{LM} \rangle}{\langle \mathcal{MM} \rangle}. \tag{25}$$

In the current work, only global averaging operations for the finite difference schemes are considered such that the *dynamic coefficient* is calculated as

$$c_{k,n}^{dyn} = c_{k,n}^{*} \frac{\left\langle \left|\frac{\delta^{k+n}\bar{u}}{\delta x^{k+n}}\right|^{\Delta^2} - \frac{\alpha^k(1-\alpha^2)}{1-\alpha^k} f c_{2,k+n}^{*} \Delta^2 \left|\frac{\delta^{k+n+2}\bar{u}}{\delta x^{k+n+2}}\right|^{\Delta} \left|\frac{\delta^{k+n}\bar{u}}{\delta x^{k+n}}\right|^{\Delta} \right\rangle}{\left\langle \left(\left|\frac{\delta^{k+n}\bar{u}}{\delta x^{k+n}}\right|^{\Delta} - \frac{\alpha^k(1-\alpha^2)}{1-\alpha^k} f c_{2,k+n}^{*} \Delta^2 \left|\frac{\delta^{k+n+2}\bar{u}}{\delta x^{k+n+2}}\right|^{\Delta} \right)^2 \right\rangle}. \tag{26}$$

Once $c_{k,n}^{dyn}$ is calculated, its value can be used in the optimized implicit finite difference approximation

$$\sum_{l=-q}^{q} \alpha_l \overline{\frac{\partial^n u}{\partial x^n}}(x_{i+l}) = \sum_{j=-r}^{r} \frac{\beta_j}{\Delta^n} \bar{u}(x_{i+j}) + c_{k,n}^{dyn} \Delta^k \left|\frac{\delta^{k+n}\bar{u}}{\delta x^{k+n}}\right|^{\Delta} + \mathcal{O}(\Delta^k). \tag{27}$$

Eq. (27) is useful in case of explicit dynamic finite difference schemes ($q = 0$ and $\alpha_0 = 1$). Formulation (27), however, undermines the advantageous philosophy of compact Padé schemes. Indeed, using an explicit finite difference approximation for the $(k+n)$th derivative results into an implicit scheme with a larger explicit stencil width than strictly required for this order of accuracy. This can be remedied by substituting the explicit $(k+n)$th derivative by an implicit formulation, which is equivalent of writing (27) immediately in its most compact formulation. Obviously, the latter approach is less complicated than the elaborate construction of an implicit formulation of the $(k+n)$th derivative. Hence, consider respectively the incompact and compact $(k+2)$nd-order implicit finite difference approximations

$$\sum_{l=-q}^{q} \alpha_l \overline{\frac{\partial^n u}{\partial x^n}}(x_{i+l}) = \sum_{j=-r}^{r} \frac{\beta_j}{\Delta^n} \bar{u}(x_{i+j}) + c_{k,n}^{*} \Delta^k \left|\frac{\delta^{k+n}\bar{u}}{\delta x^{k+n}}\right|^{\Delta} + \mathcal{O}(\Delta^{k+2}), \tag{28}$$

$$\sum_{l=-q}^{q} \alpha'_l \overline{\frac{\partial^n u}{\partial x^n}}(x_{i+l}) = \sum_{j=-r-1}^{r+1} \frac{\beta'_j}{\Delta^n} \bar{u}(x_{i+j}) + \mathcal{O}(\Delta^{k+2}). \tag{29}$$

Subtracting both expressions (28) and (29) and multiplying the resulting relation by the factor $c_{k,n}^{dyn}/c_{k,n}^{*}$ gives

$$c_{k,n}^{dyn} \Delta^k \left|\frac{\delta^{k+n}\bar{u}}{\delta x^{k+n}}\right|^{\Delta} = \frac{c_{k,n}^{dyn}}{c_{k,n}^{*}} \left[\sum_{l=-q}^{q} (\alpha_l - \alpha'_l) \overline{\frac{\partial^n u}{\partial x^n}}(x_{i+l}) \right] + \frac{c_{k,n}^{dyn}}{c_{k,n}^{*}} \left[\sum_{j=-r-1}^{r+1} \frac{\beta'_j}{\Delta^n} \bar{u}(x_{i+j}) - \sum_{j=-r}^{r} \frac{\beta_j}{\Delta^n} \bar{u}(x_{i+j}) \right] + \mathcal{O}(\Delta^{k+2}), \tag{30}$$

substitution of which in Eq. (27) yields,

$$\sum_{l=-q}^{q} \left[\alpha_l - \frac{c_{k,n}^{dyn}}{c_{k,n}^{*}} (\alpha_l - \alpha'_l) \right] \overline{\frac{\partial^n u}{\partial x^n}}(x_{i+l}) = \sum_{j=-r}^{r} \frac{\beta_j}{\Delta^n} \left[1 - \frac{c_{k,n}^{dyn}}{c_{k,n}^{*}} \right] \bar{u}(x_{i+j}) + \frac{c_{k,n}^{dyn}}{c_{k,n}^{*}} \sum_{j=-r-1}^{r+1} \frac{\beta'_j}{\Delta^n} \bar{u}(x_{i+j}) + \mathcal{O}(\Delta^k). \tag{31}$$

Although for the higher derivatives in (26) again compact Padé schemes may be used, in this work they are obtained using explicit approximations for reasons of simplicity. The resulting dynamic scheme (31) has a formal order of accuracy k unless $c_{k,n}^{dyn} = c_{k,n}^{*}$, which would lead to the formal order of accuracy $k+2$.

The present investigation focusses on the performance of three such schemes in large-eddy simulation, i.e. the 4th-order implicit tridiagonal dynamic finite difference scheme, and the 2nd-order and 4th-order explicit dynamic finite difference schemes which are a subclass of the implicit methods. These finite difference approximations are described in detail in Appendix A.

3.6. The role of the blending factor

In the previous, the blending factor f was introduced rather *ad hoc* in order to justify the extraction of the dynamic coefficient $c_{k,n}^{dyn}$ from Eqs. (10) and (11). In the following, the role of f is further clarified by performing an asymptotic perturbation analysis on the expression (26) for the dynamic coefficient. Consider therefore a very smooth field $\bar{u}(x)$ for which $\kappa_c/\kappa_{max} \to 0$ such that the difference (16) may be assumed negligible, i.e. $\mathcal{E} \approx 0$. The dynamic coefficient is then readily obtained from (16) as

$$c_{k,n}^{dyn} \approx -\frac{\mathcal{L}}{\mathcal{M}} \tag{32}$$

and can be reformulated as

$$c_{k,n}^{dyn} \approx c_{k,n}^{*} \frac{1}{1-\epsilon}, \quad \epsilon = \frac{\mathcal{L} + c_{k,n}^{*}\mathcal{M}}{\mathcal{L}}, \tag{33}$$

in which the perturbation $\epsilon \approx \frac{c_{k,n}^{dyn} - c_{k,n}^{*}}{c_{k,n}^{dyn}}$ has a value close to zero since $\mathcal{L} \approx -c_{k,n}^{*}\mathcal{M}$ for $\kappa_c/\kappa_{max} \to 0$. Expanding expression (33) into the MacLaurin series then yields

$$c_{k,n}^{dyn} \approx c_{k,n}^{*} \sum_{m=0}^{\infty} \epsilon^{m}. \tag{34}$$

Truncation of the infinite series in (34) to $m = 2$ and substitution into expression (27) gives the finite difference approximation

$$\sum_{l=-q}^{q} \alpha_l \overline{\frac{\partial^n u}{\partial x^n}}(x_{i+l}) = \sum_{j=-r}^{r} \frac{\beta_j}{\Delta^n} \bar{u}(x_{i+j}) + c_{k,n}^{*}\Delta^k \frac{\delta^{k+n}\bar{u}}{\delta x^{k+n}}\bigg|^{\Delta} + \frac{\alpha^k(1-\alpha^2)}{1-\alpha^k} f^{*} c_{k,n}^{*} c_{2,k+n}^{*} \Delta^{k+2} \frac{\delta^{k+n+2}\bar{u}}{\delta x^{k+n+2}}\bigg|^{\Delta} + \mathcal{O}(\Delta^{k+4}), \tag{35}$$

where f^{*} denotes the asymptotic value of the blending factor f for $\kappa_c/\kappa_{max} \to 0$. The value of f^{*} is then determined by writing out the Taylor series expansion of expression (7) up to the order $\mathcal{O}(\Delta^{k+4})$, such that

$$\sum_{l=-q}^{q} \alpha_l \overline{\frac{\partial^n u}{\partial x^n}}(x_{i+l}) = \sum_{j=-r}^{r} \frac{\beta_j}{\Delta^n} \bar{u}(x_{i+j}) + c_{k,n}^{*}\Delta^k \left\{ \frac{\delta^{k+n}\bar{u}}{\delta x^{k+n}}\bigg|^{\Delta} + \sum_{k'=2}^{\infty} c_{k',k+n}^{*} \Delta^{k'} \overline{\frac{\partial^{k'+k+n} u}{\partial x^{k'+k+n}}} \right\} + c_{k+2,n}^{*}\Delta^{k+2} \overline{\frac{\partial^{k+n+2} u}{\partial x^{k+n+2}}} + \mathcal{O}(\Delta^{k+4}). \tag{36}$$

Identifying the corresponding terms in (35) and (36) finally gives

$$f^{*} = \frac{1-\alpha^k}{\alpha^k(1-\alpha^2)} \frac{c_{k+2,n}^{*} + c_{k,n}^{*} c_{2,k+n}^{*}}{c_{k,n}^{*} c_{2,k+n}^{*}}. \tag{37}$$

For this value of f^{*}, expression (35) represents a standard finite difference approximation of order $\mathcal{O}(\Delta^{k+4})$. Obviously, an analogous relation can be obtained for the fully implicit expression (31) instead of (27). Note that if the blending factor $f \neq f^{*}$, then the order of accuracy in (35) reduces to $\mathcal{O}(\Delta^{k+2})$. Moreover, it will be shown in Section 4.2, that in case $\kappa_c/\kappa_{max} > 0$, an optimal value $f > f^{*}$ can be found such that the global dispersion relation of the dynamic finite difference scheme is minimized a priori for all scales up to the ratio $\kappa_c/\kappa_{max} > 0$.

In further discussions it will be shown that the kth-order dynamic finite difference scheme may be advantageous in comparison with the $(k+2)$nd-order standard scheme and the kth-order Dispersion-Relation Preserving scheme, despite its small additional cost due to the evaluation the dynamic coefficient (26). Although the expression (26) for the dynamic coefficient requires the evaluation of the $(k+n+2)$nd derivative, it might suffice to determine this coefficient only each few iterations. Hence, the cost will then be comparable with that of the $(k+2)$nd-order standard scheme and the kth-order Dispersion-Relation Preserving scheme and lower than that of the static Dispersion-Relation Preserving $(k+2)$nd-order scheme in which, e.g. the $(k+n+2)$nd derivative must be evaluated every iteration.

4. Fourier analysis and high-Reynolds calibration

4.1. Fourier transformation

In this section, a Fourier analysis is performed on the selected explicit and implicit dynamic finite difference approximations for the nth derivative. The following Fourier analysis focusses in particular on the dynamic coefficient since this coefficient is considered crucial for obtaining good quality of the optimized finite difference approximation. The nth finite difference derivative is represented in Fourier space as

$$\mathcal{F}\left\{\frac{\delta^n \bar{u}}{\delta x^n}\right\} = (i\kappa_n')^n \mathcal{F}\{\bar{u}\}, \tag{38}$$

where κ_n' denotes the modified wavenumber. Note that the real part of the modified wavenumber κ_n' represents dispersion errors, whereas the imaginary part represents dissipation errors which are absent in the current symmetric or central finite difference approximations. The expressions for the modified wavenumber of the implicit finite difference approximation (31) yield,

$$\kappa_n'^{n}(\kappa) = \frac{1}{i^{n-1}} \frac{\sum_{j=0}^{r} \gamma_j \sin(j\kappa\Delta) + \sum_{j=0}^{r+1} \gamma_j' \sin(j\kappa\Delta)}{\sum_{l=0}^{q} \eta_l \cos(l\kappa\Delta)}, \quad \forall n \in 2\mathbb{N}+1 \tag{39}$$

$$\kappa_n'^{n}(\kappa) = \frac{1}{i^{n}} \frac{\sum_{j=0}^{r} \gamma_j \cos(j\kappa\Delta) + \sum_{j=0}^{r+1} \gamma_j' \cos(j\kappa\Delta)}{\sum_{l=0}^{q} \eta_l \cos(l\kappa\Delta)}, \quad \forall n \in 2\mathbb{N}, \tag{40}$$

where the coefficients γ_l and γ_l' are determined by

$$\gamma_0 = \beta_0\left[1 - \frac{c_{k,n}^{dyn}}{c_{k,n}^*}\right], \quad \gamma_0' = \beta_0' \frac{c_{k,n}^{dyn}}{c_{k,n}^*}, \quad \forall n, \tag{41}$$

$$\gamma_j = 2\beta_j\left[1 - \frac{c_{k,n}^{dyn}}{c_{k,n}^*}\right], \quad \gamma_j' = 2\beta_j' \frac{c_{k,n}^{dyn}}{c_{k,n}^*}, \quad \forall n, \forall j > 0, \tag{42}$$

whereas η_l are obtained by

$$\eta_0 = \alpha_0 - \frac{c_{k,n}^{dyn}}{c_{k,n}^*}(\alpha_0 - \alpha_0'), \quad \forall n, \tag{43}$$

$$\eta_l = 2\alpha_l - 2\frac{c_{k,n}^{dyn}}{c_{k,n}^*}(\alpha_l - \alpha_l'), \quad \forall n, \forall l > 0. \tag{44}$$

Obviously $\mathcal{O}(\Delta^{k+2})$ is recovered if $c_{k,n}^{dyn}$ equals the theoretical value $c_{k,n}^*$ obtained from Taylor expansion. Nevertheless, it is clear by now that the actual value of the coefficient $c_{k,n}^{dyn}$ will depend on the nature of the resolved field $\bar{u}(x)$, its derivatives and the value of the blending factor f. Hence, the spectral behaviour of $c_{k,n}^{dyn}$ will heavily influence the behaviour of the modified wavenumber, and further analysis is inevitable. Since the spectral content of the flow field is mostly reflected by the energy spectrum, an attempt is made to analyze the behaviour of the dynamic coefficient by transforming the error definition into Fourier space. Using $\hat{}$ to denote the Fourier transform, the error definition (16) is transformed to Fourier space as

$$\widehat{\mathcal{E}}(\kappa) = \widehat{\mathcal{L}} + c_{k,n}\widehat{\mathcal{M}}, \tag{45}$$

with $c_{k,n}$ the *constant dynamic coefficient* and

$$\widehat{\mathcal{L}}(\kappa) = c_{k,n}^*(\alpha^k - 1)\Delta^k(i\kappa_{k+n}')^{k+n}\hat{u}, \tag{46}$$

$$\widehat{\mathcal{M}}(\kappa) = (1-\alpha^k)\Delta^k(i\kappa_{k+n}')^{k+n}\hat{u} - \alpha^k(1-\alpha^2)\Delta^{k+2}fc_{2,k+n}^*(i\kappa_{k+n+2}')^{k+n+2}\hat{u}, \tag{47}$$

corresponding to Eqs. (22) and (23). Using expression (45), an error spectrum is defined as (* denotes the complex conjugate)

$$E_{\widehat{\mathcal{E}}}(\kappa) = \widehat{\mathcal{E}}\widehat{\mathcal{E}}^* = \widehat{\mathcal{L}}\widehat{\mathcal{L}}^* + c_{k,n}\widehat{\mathcal{M}}\widehat{\mathcal{L}}^* + c_{k,n}\widehat{\mathcal{M}}^*\widehat{\mathcal{L}} + c_{k,n}^2\widehat{\mathcal{M}}\widehat{\mathcal{M}}^*. \tag{48}$$

Since the basic order of accuracy k is even for central schemes, it can be verified that in that case $\widehat{\mathcal{M}}\widehat{\mathcal{L}}^* = \widehat{\mathcal{M}}^*\widehat{\mathcal{L}}$ and thus

$$E_{\widehat{\mathcal{E}}}(\kappa) = \widehat{\mathcal{E}}\widehat{\mathcal{E}}^* = \widehat{\mathcal{L}}\widehat{\mathcal{L}}^* + 2c_{k,n}\widehat{\mathcal{M}}\widehat{\mathcal{L}}^* + c_{k,n}^2\widehat{\mathcal{M}}\widehat{\mathcal{M}}^*. \tag{49}$$

The optimal value for the coefficient $c_{k,n}$ can now be found by a least square approximation in Fourier space, defined as

$$\frac{\partial}{\partial c_{k,n}}\int_0^{\frac{\pi}{\Delta}} E_{\widehat{\mathcal{E}}}(\kappa)d\kappa = 0. \tag{50}$$

Working out this integral expression leads to following expression for the ratio $c_{k,n}^{dyn}/c_{k,n}^*$

$$\frac{c_{k,n}^{dyn}}{c_{k,n}^*} = \frac{\int_0^{\frac{\pi}{\Delta}}(\kappa_{k+n}')^{k+n}\left[(\kappa_{k+n}')^{k+n} + \frac{\alpha^k(1-\alpha^2)}{1-\alpha^k}\Delta^2 fc_{2,k+n}^*(\kappa_{k+n+2}')^{k+n+2}\right]\hat{u}\hat{u}^*\,d\kappa}{\int_0^{\frac{\pi}{\Delta}}\left[(\kappa_{k+n}')^{k+n} + \frac{\alpha^k(1-\alpha^2)}{1-\alpha^k}\Delta^2 fc_{2,k+n}^*(\kappa_{k+n+2}')^{k+n+2}\right]^2\hat{u}\hat{u}^*\,d\kappa}, \tag{51}$$

in which the product $\hat{u}\hat{u}^*$ represents the energy spectrum $E_u(\kappa)$ of the flow field $u(x)$. Hence, the ratio $c_{k,n}^{dyn}/c_{k,n}^*$ is entirely determined by the value of the blending factor f and the instantaneous energy spectrum of the flow field. Obviously, the instantaneous energy spectrum is characterized by a specific shape and a filter-to-grid cutoff ratio κ_c/κ_{max} which can vary in time. Once these parameters are defined, it is possible to calculate the ratio $c_{k,n}^{dyn}/c_{k,n}^*$ from the integral expression (51) and substitute it into the expression of the modified wavenumber (39) or (40). The behaviour of expression (51) as function of these parameters was already investigated in previous work [13]. We briefly repeat here the main conclusions.

1. It follows readily from Eq. (51) that the dynamic coefficient $c_{k,n}^{dyn}$ recovers the Taylor value $c_{k,n}^*$ if $f = 0$, regardless the filter-to-grid cutoff-ratio κ_c/κ_{max}.
2. For the limit $\kappa_c/\kappa_{max} \to 0$, i.e. for very smooth fields $\bar{u}(x)$ at $\mathrm{Re} \to 0$ which contain only few Fourier modes, the dynamic coefficients always converge to the theoretical Taylor value $c_{k,n}^*$ regardless of the value of the blending factor. This means that each dynamic finite difference approximation recovers the asymptotic order of accuracy $\mathcal{O}(\Delta^{k+2})$ for very smooth fields.[4]

[4] Remark that in case of a constant field $\bar{u}(x)$ for which $\kappa_c/\kappa_{max} = 0$, expression (51) reduces to 0/0, and the dynamic coefficient $c_{k,n}^{dyn}$ becomes *indefinite*. This makes sense since any finite difference approximation is exact for a constant. Hence, this particularity can be safely avoided by setting $c_{k,n}^{dyn} = 0$ or $c_{k,n}^{dyn} = c_{k,n}^*$ as soon as $\mathcal{L} = 0$ and $\mathcal{M} = 0$.

3. The ratio $c_{k,n}^{dyn}/c_{k,n}^{*}$ has to meet specific conditions in order to obtain the desired spectral characteristics. It was observed in Fauconnier et al. [13] that if $0 \leqslant c_{k,n}^{dyn}/c_{k,n}^{*} < 1$, the scheme's Fourier characteristic will lie between that of the kth-order and $(k+2)$nd-order standard scheme. Moreover, if $c_{k,n}^{dyn}/c_{k,n}^{*} < 0$, poor Fourier characteristics are observed that lie below that of the kth-order scheme. Hence, it is necessary that $c_{k,n}^{dyn}/c_{k,n}^{*} \geqslant 1$ for all values of the wavenumber ratio κ_c/κ_{max}. Further, $c_{k,n}^{dyn}/c_{k,n}^{*}$ acts like a sensor for the spectral content in the flow field $\bar{u}$. It should therefore be a monotonic function of the filter-to-grid cutoff-ratio κ_c/κ_{max} such that each value of $c_{k,n}^{dyn}$ corresponds to a unique value of $\frac{\kappa_c}{\kappa_{max}}$. Both previous conditions are mathematically expressed by

$$\frac{c_{k,n}^{dyn}}{c_{k,n}^{*}} \geqslant 1, \tag{52}$$

$$\frac{1}{c_{k,n}^{*}}\frac{\partial c_{k,n}^{dyn}}{\partial \kappa} \geqslant 0, \quad \forall \kappa. \tag{53}$$

Obviously the restrictions (52) and (53) can be achieved by choosing a proper value of f.

In the following section, the optimal value of the blending factor f will be determined by calibrating the modified wavenumber for a turbulent spectrum at $\mathrm{Re} \to \infty$ with fixed filter-to-grid cutoff ratio κ_c/κ_{max}, such that the dispersion errors are minimal in the range $[0, \kappa_c/\kappa_{max}]$. The obtained value of f will merely guarantee that the dynamic scheme reaches maximum performance for a large-eddy simulation at high Reynolds numbers with a maximum filter-to-grid cutoff ratio κ_c/κ_{max}. Moreover, in case of low Reynolds numbers or in case of direct numerical simulations, where the smallest resolved scales or *Kolmogorov scales* κ_η are smaller than κ_c, the ratio $c_{k,n}^{dyn}/c_{k,n}^{*}$ is expected to adapt such that the dispersion errors are close to the minimum in the range $[0, \kappa_\eta/\kappa_{max}]$.

4.2. Calibration for $\mathrm{Re} \to \infty$

In analogy with previous work [13], the optimal value of the blending factor f is determined by minimizing the kinetic energy associated to the resulting finite difference error. This way, the energy spectrum of the flow is taken into account as a natural weighting function. Although the method is similar to the traditional methods used by, e.g. Tam and Webb [8] or Kim and Lee [9], the weighting function in the current method has a clear meaning, rather than being an ad hoc function.

The spectral error between the exact nth derivative and a dynamic finite difference approximation with modified wavenumber κ_n', is defined as

$$\widehat{\mathcal{E}}(\kappa) = i^n(\kappa^n - \kappa_n'^{\,n}(\kappa, f))\Delta^n \hat{u}. \tag{54}$$

The related error spectrum is then determined as

$$E_{\widehat{\mathcal{E}}}(\kappa) = \widehat{\mathcal{E}}\widehat{\mathcal{E}}^{*} = (\kappa^n - \kappa_n'^{\,n}(\kappa, f))^2 \Delta^{2n} E_u(\kappa), \tag{55}$$

where $E_u(\kappa)$ represents the energy spectrum of the flow field $u(x)$ given by the product $\hat{u}\hat{u}^{*}$. The optimal value for the blending factor f can be calculated by finding the minimum of the integral over all wave components, i.e. by solving

$$\frac{\partial}{\partial f}\int_0^{\frac{\pi}{\Delta}} (\kappa^n - \kappa_n'^{\,n}(\kappa, f))^2 E_u(\kappa) d\kappa = 0. \tag{56}$$

In the following, the integral in (56) is solved numerically by assuming a model spectrum. Hence, an idealized inertial range spectrum for homogeneous isotropic turbulence is introduced, that is defined as

$$E_u(\kappa) = [1 - H(\kappa - \kappa_c)]\kappa^{-\beta} = \begin{cases} \kappa^{-\beta} & \kappa < \kappa_c, \\ 0 & \kappa > \kappa_c, \end{cases} \tag{57}$$

where β determines the slope of the inertial range and the cutoff wavenumber κ_c indicates the highest appearing wavenumber in the (resolved) field $\bar{u}(x)$. Since the purpose of this simplified energy spectrum is solely to mimic the distribution of the turbulent energy spectrum at $\mathrm{Re} \to \infty$, no attempt is undertaken to model the *energy containing range* nor the *dissipation range*. Indeed, it is expected that the influence of the non-universal energy containing range is negligible since it is restricted to the largest resolved scales at small κ/κ_{max}, which are approximated sufficiently accurate by most discretization schemes. The dissipation range is also not taken into account, since $\mathrm{Re} \to \infty$ implies that the inertial range extends to infinity and thus no dissipation range occurs.

For the optimization of the blending factor f, a specific inertial range slope must be selected. Since the dynamic finite difference schemes will be applied to the Navier–Stokes equations, the appropriate slopes that correspond to that of the inertial range of respectively the turbulent velocity $\bar{\mathbf{u}}(\mathbf{x})$ and the turbulent pressure field $\bar{p}(\mathbf{x})$ must be considered. Indeed, the Navier–Stokes equations contain, besides the various discrete derivatives of the velocity field, the finite difference

approximation of the pressure gradient which must also be optimized. The energy spectrum of the pressure in homogeneous isotropic turbulence is found to have a finite inertial range that scales with $\kappa^{-7/3}$ and is followed by a bump of nearly $\kappa^{-5/3}$ at higher wave numbers [18].

Hence, the optimization of the finite difference approximations for the pressure derivatives must be calibrated using a $\kappa^{-7/3}$ generic spectrum, whereas the optimization of the finite difference approximations of the velocity derivatives must be calibrated with Kolmogorov's $\beta = -5/3$ scaling for the velocity field.

Note that one could also consider a separate optimization of the finite difference approximations for the derivatives of the turbulent viscosity, which is needed for the evaluation of the subgrid force, and which requires the spectrum of, e.g. the strain-rate magnitude in the Smagorinsky model. However, such an optimization would lead to a lot of extra complexity in the scheme without much benefit, and the blending factors for the derivative of the turbulent viscosity are therefore assumed to be the same as for the velocity field.

Fig. 2 displays the optimal blending factors f as function of κ_c/κ_{max} for the inertial range spectrum (57) with $\beta = -5/3$ and $\beta = -7/3$. The behaviour of the optimal blending factor is illustrated for the 2nd- and 4th-order explicit linear dynamic schemes and the 4th-order tridiagonal implicit dynamic scheme, which will be the subject of investigation in this work (see Appendix A). Remark that the optimal value of f depends on the wavenumber range one wants to optimize for, indicated by κ_c. In the present work, the large-eddy simulation framework with the double decomposition and sharp cutoff filtering is considered such that all modes in the range $\frac{2}{3}\kappa_{max} < \kappa_c < \kappa_{max}$ are filtered out in order to prevent aliasing errors [6]. Therefore, the blending factor f was not determined in this high-wavenumber range. Notice that for $\kappa_c/\kappa_{max} \to 0$, the optimal blending factor tends to the asymptotic value f^*, which can be determined via expression (37). For the explicit schemes, the value of $f^* = 0.2$ for the 1st and 2nd derivative, whereas $f^* = 0.089$ and $f^* = 0.1041$ for respectively the 1^{st} and 2nd derivative of the 4th-order implicit scheme. As already mentioned, it is highly desirable in large-eddy simulation to resolve as much scales of motion, as accurately as possible, on a certain computational grid (more specific all scales up to the dealiasing cutoff $\kappa_c = \frac{2}{3}\kappa_{max}$). Hence, in this work we prefer to determine the optimal value of the blending factors in the dynamic schemes for the inertial range spectrum (57) with cutoff wavenumber $\kappa_c = \frac{2}{3}\kappa_{max}$. Nevertheless, we will also investigate the performance of the dynamic schemes for the asymptotic value f^* of the blending factor. Fig. 3 shows the spectral behaviour of the dynamic coefficient of the 4th-order explicit scheme for both choices of the blending factor, assuming the model spectrum with $\beta = -\frac{5}{3}$. Table 1 gives the values of the optimal blending factors f and the corresponding coefficients $c_{k,n}^{dyn}$ for the inertial range spectra (57) with $\kappa_c = \frac{2}{3}\kappa_{max}$ and $\beta = -5/3$ and $\beta = -7/3$. Fig. 3 clearly indicates that no extreme and inappropriate values for the dynamic coefficient occur, as long as the adopted value of the blending factor f is realistic, i.e. restricted to the interval $\left[f^*, f\left(\frac{2}{3}\kappa_{max}\right)\right]$. Hence, the dynamic schemes are expected to remain stable during simulation regardless the spectral content on the computational grid, and thus no additional clipping on the dynamic coefficients is required. Since it is not always desirable to optimize finite difference schemes in the entire wavenumber range (because of the large dispersion errors which occur in $\frac{2}{3}\kappa_{max} < \kappa_c < \kappa_{max}$), one may decide to limit the dynamic coefficient nevertheless to a maximum value, e.g. the value at the cutoff wavenumber $\kappa_c = \frac{2}{3}\kappa_{max}$. Such an approach could be useful in practical simulations where typically no de-aliasing filter is applied and Fourier modes appear in the entire wavenumber range. In this work, however, all Fourier modes in the range $\frac{2}{3}\kappa_{max} < \kappa_c < \kappa_{max}$ are filtered out, making such a limitation redundant.

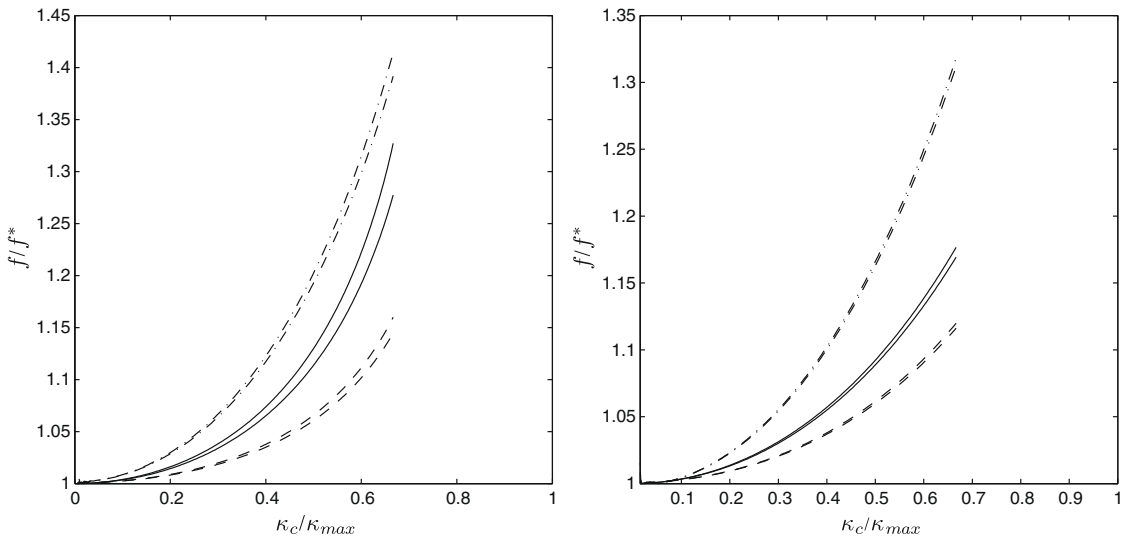

Fig. 2. The optimal blending factors f as function of κ_c/κ_{max}. First derivative $n = 1$ (left) and second derivative $n = 2$ (right). (—) 2nd-order explicit with $f^* = 0.2$ for $n = 1, 2$; (– – –) 4th-order explicit with $f^* = 0.2$ for $n = 1, 2$; (-·-·-) 4th-order tridiagonal Padé with $f^* = 0.089$ for $n = 1$ and $f^* = 0.1041$ for $n = 2$. The upper curves correspond to the model spectrum with $\beta = -\frac{7}{3}$, whereas the lower curves correspond to the model spectrum with $\beta = -\frac{5}{3}$.

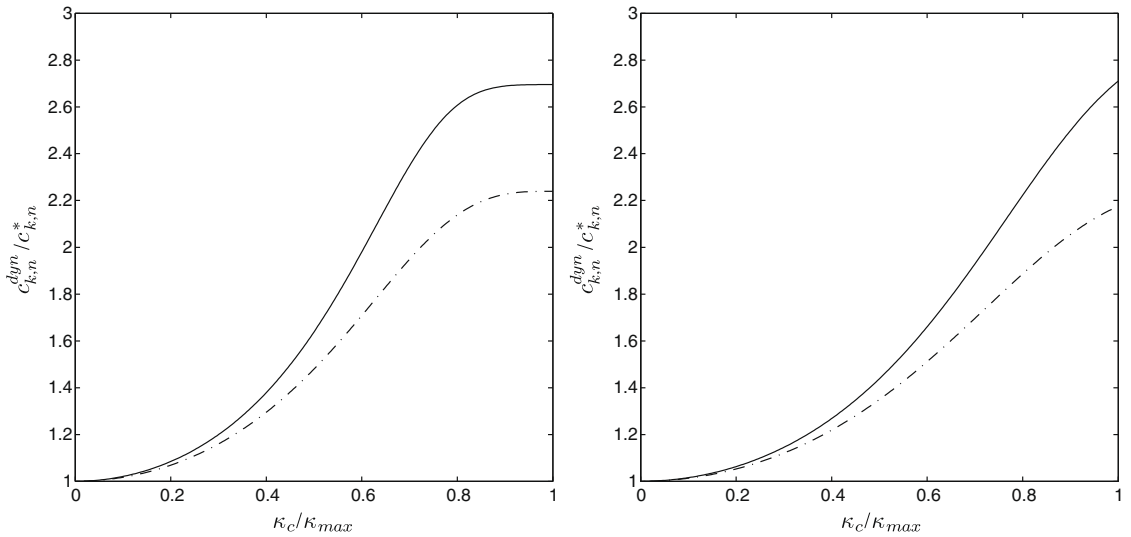

Fig. 3. Ratio of the dynamic coefficient to its Taylor value $c^{dyn}_{k,n}/c^{*}_{k,n}$ for the 4th-order explicit scheme ($k = 4$) as function of the cutoff wavenumber ratio κ_c/κ_{max}. $\beta = -\frac{5}{3}$ was assumed in the model spectrum. First derivative $n = 1$ (left) and second derivative $n = 2$ (right). The straight line (—) corresponds to $c^{dyn}_{k,n}/c^{*}_{k,n}$ where $f = f(\kappa_c = \frac{2}{3}\kappa_{max})$, whereas the dash-dot line (-·-·) corresponds to $c^{dyn}_{k,n}/c^{*}_{k,n}$ with $f^{*} = f(\kappa_c = 0)$.

4.3. Dispersion-Relation Preserving schemes

Clearly, the dynamic finite difference approximations act as a *k*th-order Dispersion-Relation Preserving schemes of, e.g. Tam and Webb [8] due to the optimization of the parameter $c^{dyn}_{k,n}/c^{*}_{k,n}$. However, the optimal value of the ratio $c^{dyn}_{k,n}/c^{*}_{k,n}$ is not determined a priori, but is obtained dynamically from expressions (26), according to the instantaneous spectral content of the flow and the a priori choice of a blending factor *f*. In the present study, the Dispersion-Relation Preserving (DRP) schemes are constructed by determining immediately an a priori optimal value for the ratio $c^{dyn}_{k,n}/c^{*}_{k,n}$ instead of an optimal blending factor *f*. Since most often, the uniform inertial range spectrum with slope $\beta = 0$ is implicitly assumed for the construction of DRP schemes, e.g. [8], it is also used for the derivation of these schemes in this paper. Table 1 gives an overview of the values of the coefficients $c_{k,n}$ for the uniform energy spectrum at $\kappa_c = \frac{2}{3}\kappa_{max}$.

4.4. Fourier characteristics

Figs. 4–6 display, respectively, the error on the modified wavenumbers ($n = 1, 2$) for the 2nd- and 4th-order explicit dynamic schemes and the 4th-order dynamic Padé scheme (as described in Appendix A). For the determination of the constant dynamic coefficient, the inertial range spectrum (57) with slope $\beta = -5/3$ and a filter-to-grid cutoff-ratio $\frac{\kappa_c}{\kappa_{max}} = \frac{2}{3}$ are assumed. It is observed from the figures that the spectral characteristics of the dynamic schemes are close to that of their Dispersion-Relation Preserving counterparts, especially for the higher-order schemes like the 4th-order dynamic Padé scheme, were the curves almost collapse. This indicates that the slope of the energy spectrum becomes less important in the optimization procedure in case of higher-order basic schemes, since these schemes perform already well. This observation is confirmed by the values of the dynamic coefficients in Table 1 for various slopes β.

Table 1
Numerically obtained optimal blending factors f and corresponding values of $c^{dyn}_{k,n}$ for the inertial range model spectrum at $\kappa_c = \frac{2}{3}\kappa_{max}$.

Slope	Scheme	$n = 1$		$n = 2$	
		f	$c^{dyn}_{k,1}$	f	$c^{dyn}_{k,2}$
$\beta = -\frac{5}{3}$	Explicit $k = 2$	0.2555	−0.3088	0.2339	−0.1310
	Explicit $k = 4$	0.2298	0.0740	0.2241	0.0203
	Implicit $k = 4$	0.1241	0.0121	0.1363	0.0069
$\beta = -\frac{7}{3}$	Explicit $k = 2$	0.2654	−0.2966	0.2353	−0.1293
	Explicit $k = 4$	0.2329	0.0724	0.2248	0.0201
	Implicit $k = 4$	0.1261	0.0120	0.1370	0.0069
$\beta = 0$	Explicit $k = 2$		−0.3344		−0.1345
	Explicit $k = 4$		0.0775		0.0206
	Implicit $k = 4$		0.0119		0.0069

5. Taylor–Green vortex: transition into turbulence

The Taylor–Green vortex flow was selected to examine the performance of the developed dynamic finite difference approximations. The viscous Taylor–Green vortex flow, first introduced in 1937 by Taylor and Green [19], is considered as a prototype system that describes the production of small-scale eddies due to the mechanism of vortex-line stretching in homogeneous isotropic turbulence [20,14]. It is one of the simplest environments to study the breakdown process of large-scale vortices into successively smaller ones, and the resulting homogeneous isotropic turbulence. According to Brachet et al. [14], the generalized Taylor–Green vortex is defined as the periodic three-dimensional incompressible flow, governed by the Navier–Stokes equations and the continuity equation

$$\frac{\partial u_i}{\partial x_i} = 0, \tag{58}$$

$$\frac{\partial u_i}{\partial t} + u_j \frac{\partial u_i}{\partial x_j} = -\frac{\partial p}{\partial x_i} + \nu \frac{\partial^2 u_i}{\partial x_j^2}, \tag{59}$$

which develops from the initial solenoidal velocity field $\mathbf{u}(\mathbf{x}, t = 0)$ (in non-dimensional form)

$$\begin{aligned} u_1(\mathbf{x},0) &= \frac{2}{\sqrt{3}} \sin\left(\gamma + \frac{2\pi}{3}\right) \sin(x_1)\cos(x_2)\cos(x_3), \\ u_2(\mathbf{x},0) &= \frac{2}{\sqrt{3}} \sin\left(\gamma - \frac{2\pi}{3}\right) \cos(x_1)\sin(x_2)\cos(x_3), \\ u_3(\mathbf{x},0) &= \frac{2}{\sqrt{3}} \sin(\gamma)\cos(x_1)\cos(x_2)\sin(x_3). \end{aligned} \tag{60}$$

The parameter γ determines the shape and orientation of the initial anisotropic vortex structure. The initial pressure field $p(\mathbf{x}, t = 0)$, that follows from the initial solenoidal velocity field, is obtained by solving the Poisson equation, yielding

$$\begin{aligned} p(\mathbf{x},0) = p_0 &+ \frac{1-\cos(2\gamma)}{24}[\cos(2x_1)\cos(2x_2) + 2\cos(2x_3)] + \frac{2+\cos(2\gamma)+\sqrt{3}\sin(2\gamma)}{48}[\cos(2x_1)\cos(2x_3) \\ &+ 2\cos(2x_2)] + \frac{2+\cos(2\gamma)-\sqrt{3}\sin(2\gamma)}{48}[\cos(2x_2)\cos(2x_3) + 2\cos(2x_1)], \end{aligned} \tag{61}$$

where the arbitrary mean pressure component p_0 is chosen to be zero in this work.

By taking the Fourier transform of the initial velocity field (60), it can be shown that the initial condition (60) corresponds to eight Fourier modes, located at the positions $\boldsymbol{\kappa} = (\pm 1, \pm 1, \pm 1)$. Hence, condition (60) represents a single vortex scale which is located at the spherical wavenumber-shell with radius $|\kappa| = \sqrt{3}$. It was further verified that the Fourier modes related to the pressure field are located on two spherical wavenumber-shells with respective radius $|\kappa| = \sqrt{6}$ and $|\kappa| = 3$. The total amount of kinetic energy in the initial flow is obtained as

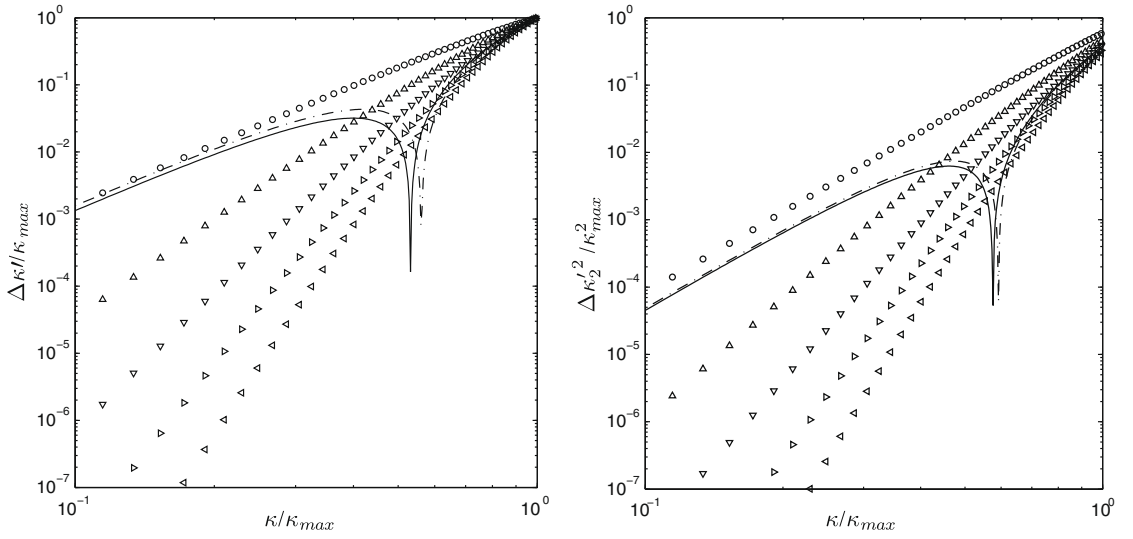

Fig. 4. Explicit dynamic finite difference approximation with $k = 2$. Error on the modified wavenumbers κ_n^m for the nth derivatives with $n = 1$ (left) and $n = 2$ (right). (○) 2nd-order central; (△) 4th-order central; (▽) 6th-order central; (▷) 8th-order central; (◁) 10th-order central; (—) explicit dynamic scheme with $k = 2(\beta = -5/3, \kappa_c = \frac{2}{3}\kappa_{max})$; (– · –·) 2nd-order DRP scheme.

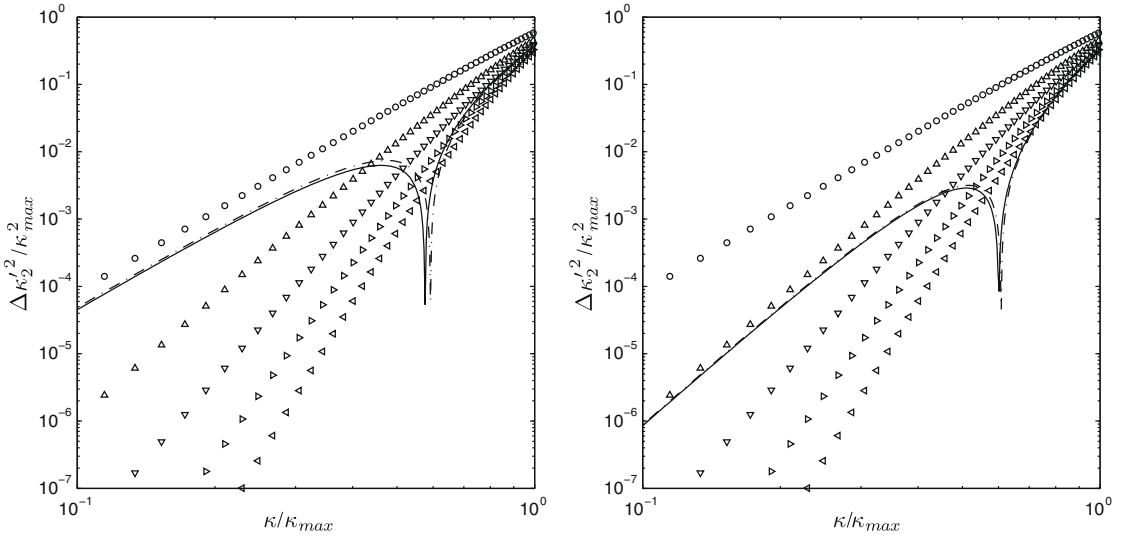

Fig. 5. Explicit dynamic finite difference approximation with $k = 4$. Error on the modified wavenumbers $\kappa_n'^m$ for the nth derivatives with $n = 1$ (left) and $n = 2$ (right). (○) 2nd-order central; (△) 4th-order central; (▽) 6th-order central; (▷) 8th-order central; (◁) 10th-order central; (—) explicit dynamic scheme with $k = 4(\beta = -5/3, \kappa_c = \frac{2}{3}\kappa_{max})$; (— · —·) 4th-order DRP scheme.

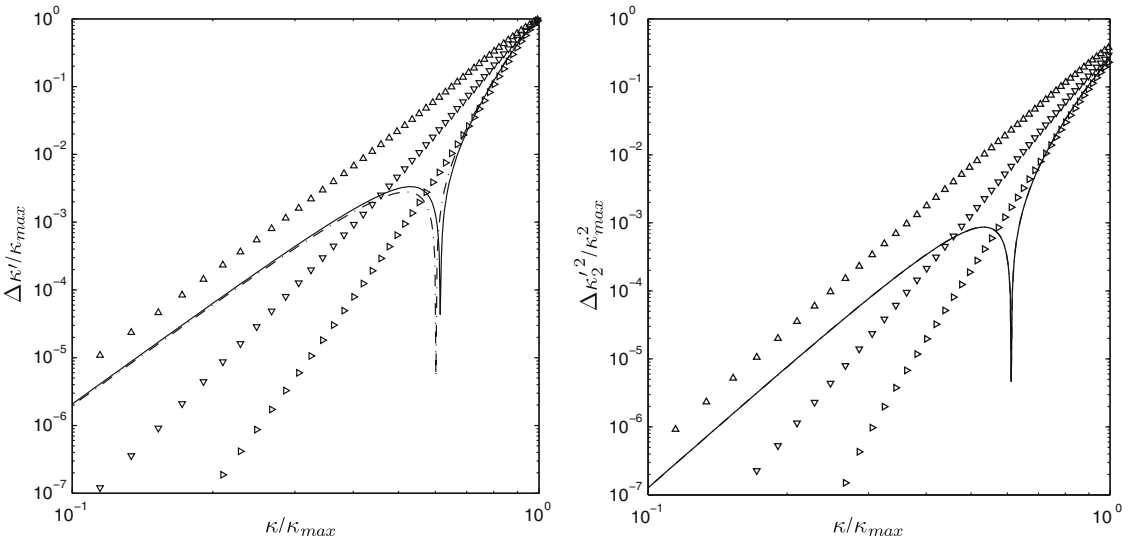

Fig. 6. Implicit dynamic finite difference approximation with $k = 4$. Error on the modified wavenumbers $\kappa_n'^m$ for the nth derivatives with $n = 1$ (left) and $n = 2$ (right). (△) 4th-order tridiagonal implicit scheme; (▽) 6th-order tridiagonal implicit scheme; (▷) 8th-order pentadiagonal implicit scheme; (—) implicit tridiagonal dynamic scheme with $k = 4$ $(\beta = -5/3, \kappa_c = \frac{2}{3}\kappa_{max})$; (— · —·) 4th-order implicit tridiagonal DRP scheme.

$$k(t=0) = \frac{1}{8\pi^3} \iiint_{\mathbf{0}}^{\mathbf{2\pi}} \frac{1}{2} u_i(\mathbf{x},0) u_i(\mathbf{x},0) d\mathbf{x} = \frac{1}{8}, \tag{62}$$

whereas the total amount of initial dissipation is obtained as

$$\varepsilon(t=0) = \frac{1}{8\pi^3} \iiint_{\mathbf{0}}^{\mathbf{2\pi}} \nu \frac{\partial u_i}{\partial x_j}(\mathbf{x},0) \frac{\partial u_i}{\partial x_j}(\mathbf{x},0) d\mathbf{x} = \frac{3}{4}\frac{1}{\mathrm{Re}}. \tag{63}$$

Brachet et al. [14] defined the Reynolds number as $\mathrm{Re} = 1/\nu$, noting that the length and velocity scales of the initial flow (60) are of order 1. In the initial stages of the simulation, the large-scale vortex flow is highly organized and thus characterized as laminar. However, the non-linear term in the Navier–Stokes equations (59) starts to generate successively smaller structures which interact with the large scales. If the Reynolds number is large enough, this results into a process of vortex-stretching and eventually into a breakdown of the large scales into smaller ones which is interpreted as turbulence. Therefore, the

Taylor–Green flow is believed to describe the fundamental process of natural transition into isotropic turbulence. This transitional behaviour is determined entirely by the choice of the Reynolds number. Brachet et al. [14] observed that for $\mathrm{Re} \geqslant 500$ the small-scale structures in the Taylor–Green flow undergo profound changes. Indeed, for high Reynolds numbers, the *turbulent* flow becomes nearly isotropic at $t = 7$ with no memory of the initial conditions, and moreover, the dissipation rate reaches a maximum at $t = 9$. However, for low Reynolds numbers, the maximum dissipation occurs earlier, whereas the flow retains some of its initial anisotropy at all times. A clear inertial range behaviour was observed once $\mathrm{Re} \geqslant 1000$. For $t \to \infty$, the isotropic turbulence, which is not maintained by an external forcing, dies out due to viscosity.

In the current work, the Reynolds number is set to $\mathrm{Re} = 1500$, which corresponds to a Reynolds number based on the transversal Taylor micro-scale $\mathrm{Re}_\lambda \approx 55$. Following Brachet et al. [14], the shape factor is chosen $\gamma = 0$. The resulting turbulent flow field is expected to exhibit an inertial range that corresponds to the Kolmogorov scaling $\kappa^{-5/3}$. In the following, the setup of the direct numerical simulation and the large-eddy simulations of the selected Taylor–Green vortex flow at $\mathrm{Re} = 1500$ is discussed. The DNS-solution will serve here as a reference solution against which the various LES-solutions are compared.

5.1. Direct numerical simulation

For the direct numerical simulation of the periodic Taylor–Green vortex flow at $\mathrm{Re} = 1500$, the system of Eqs. (58) and (59) are directly solved on a uniform computational grid with 256^3 nodes. This implies that only the first 128^3 Fourier modes in the flow field are resolved, which should be sufficient for $\mathrm{Re}_\lambda \approx 55$. These settings compare well to those of Brachet et al. [14], who used a uniform grid with $N^3 = 256^3$ for the DNS of the Taylor–Green vortex flow with Reynolds numbers up to $\mathrm{Re} = 3000$. The partial derivatives in (58) and (59) are evaluated in Fourier space by a *pseudo-spectral* method in order to exclude finite difference errors from the solution. Further, the skew-symmetric formulation is adopted for the discretization of the nonlinear term such that it conserves the kinetic energy. The Navier–Stokes equations are solved by means of the pressure-correction algorithm, in which the pressure is obtained from a Poisson equation. The time stepping is performed with the explicit low-storage 4-stage Runge–Kutta method with standard coefficients $\left[\frac{1}{4}, \frac{1}{3}, \frac{1}{2}, 1\right]$. In order to guarantee the numerical accuracy of the adopted Runge–Kutta time-stepping method, a sufficiently small time-step $\Delta t = 0.005$ was determined such that the dispersion and dissipation errors related to this method remain sufficiently low. The corresponding *Courant–Friedrichs–Lewy* number does not exceed the initial value, i.e. $\mathrm{CFL} \leqslant 0.2037$ during the simulation.

The decay of the homogeneous isotropic turbulence, that results from the Taylor–Green flow, is followed until $t = 14.25$. Fig. 7 illustrates the spectrum development of the resolved velocity field $u(x, t = t_j)$. It is seen that the energy spectrum develops from a single characteristic Fourier mode toward an entire range of modes. The temporal evolution of the decaying kinetic energy and the dissipation rate are shown in Fig. 8. It is verified that the evolution of the dissipation rate $\varepsilon(t)$ is in close agreement with that obtained by Brachet et al. [14] for $\mathrm{Re} = 1600$. One observes that the dissipation rate $\varepsilon(t)$ rises relatively sharply around $t \geqslant 4$ and reaches a maximum at $t = 9$. Brachet et al. [14] reported that the Taylor–Green flow pattern becomes heavily distorted around $t = 7$, which may be interpreted as *turbulence*. The coherent structure itself, finally breaks down around $t = 8$. Therefore, it is expected that for $t \geqslant 9$, the flow is fully turbulent and nearly-isotropic.

5.2. Large-eddy simulation

The governing equations for the large-eddy simulation are obtained by applying a convolution filter to the Navier–Stokes equations (58) and (59). In the current context of the Taylor–Green flow in a homogeneous periodic box, the homogeneous sharp cutoff filter $\mathcal{G}(\mathbf{x}, \kappa_c)$ is favoured in which the cutoff wavenumber $\kappa_c = \frac{2}{3}\kappa_{max}$ [6]. The velocity field is then decomposed as

$$\mathbf{u}(\mathbf{x}, t) = \bar{\mathbf{u}}(\mathbf{x}, t) + \mathbf{u}'(\mathbf{x}, t), \tag{64}$$

where $\bar{\mathbf{u}}(\mathbf{x}, t)$ denotes here the *low-pass* filtered velocity field (large scales) and $\mathbf{u}'(\mathbf{x}, t)$ denotes the *high-pass* filtered velocity field (small scales) such that in Fourier space

$$\hat{\bar{\mathbf{u}}}(\boldsymbol{\kappa}, t) = \widehat{\mathcal{G}}(\boldsymbol{\kappa}, \kappa_c)\hat{\mathbf{u}}(\boldsymbol{\kappa}, t) = \hat{\mathbf{u}}(\boldsymbol{\kappa}, t), \quad 0 \leqslant \boldsymbol{\kappa} \leqslant \kappa_c, \tag{65}$$

$$\hat{\mathbf{u}}'(\boldsymbol{\kappa}, t) = [1 - \widehat{\mathcal{G}}(\boldsymbol{\kappa}, \kappa_c)]\hat{\mathbf{u}}(\boldsymbol{\kappa}, t) = \hat{\mathbf{u}}(\boldsymbol{\kappa}, t), \quad \kappa_c \leqslant \boldsymbol{\kappa} \leqslant \kappa_\eta. \tag{66}$$

The filtered Navier–Stokes equations (58) and (59) are then obtained as

$$\frac{\partial \bar{u}_i}{\partial x_i} = 0, \tag{67}$$

$$\frac{\partial \bar{u}_i}{\partial t} + \frac{\partial \overline{\bar{u}_i \bar{u}_j}}{\partial x_j} + \frac{\partial \bar{\tau}_{ij}}{\partial x_j} = -\frac{\partial \bar{p}}{\partial x_i} + \nu \frac{\partial^2 \bar{u}_i}{\partial x_j^2}, \tag{68}$$

where $\bar{p}(\mathbf{x}, t)$ denotes the filtered pressure field and $\bar{\tau}_{ij} = \overline{u_i u_j} - \overline{\bar{u}_i \bar{u}_j}$ denotes the *residual-stress* tensor. Formulation (68) is typically known as the *double decomposition*. The choice of the double decomposition framework in which the nonlinear term is filtered explicitly with the sharp cutoff filter is motivated by two arguments. First, the explicit filtering up to

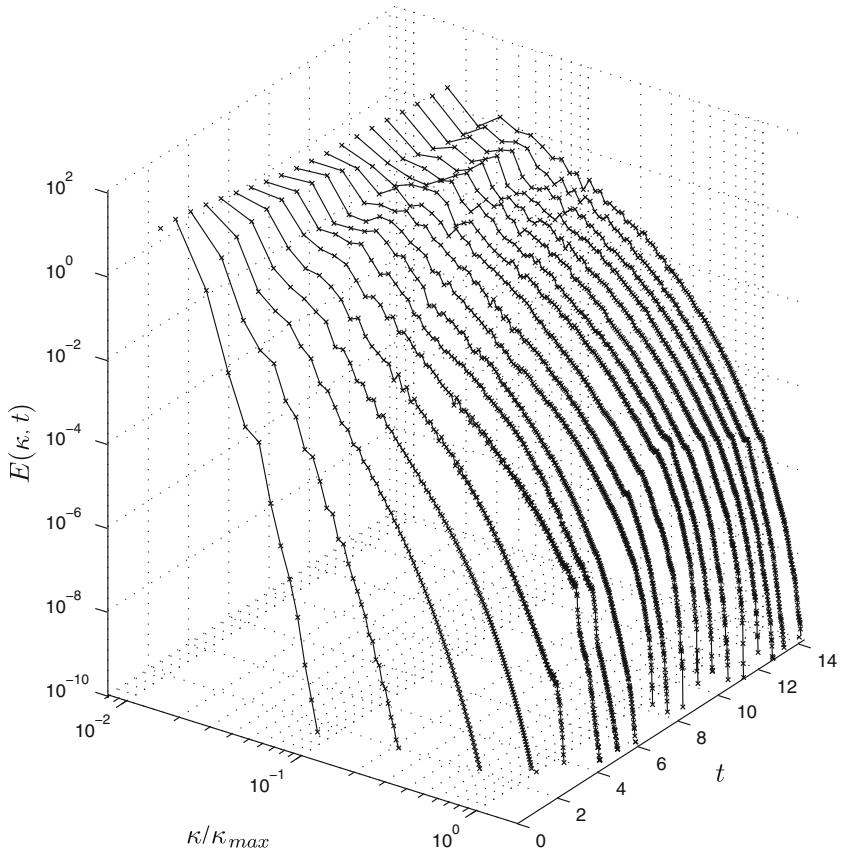

Fig. 7. Direct numerical simulation of Taylor–Green vortex. An impression of the temporal evolution of the energy spectrum $E(\kappa, t)$ in the Taylor–Green vortex flow.

$\kappa_c = \frac{2}{3}\kappa_{max}$ allows to rigorously preclude aliasing, as argued by Orszag [6]. Secondly, several authors [2–4,21–27] report that the explicit filtering procedure allows to eliminate numerical discretization errors in the high-wavenumber region $[\kappa_c, \kappa_{max}]$. Indeed, since finite difference schemes do not perform well in the wavenumber range $[\kappa_c, \kappa_{max}]$, the accuracy of the predicted scales there would be very poor.

Since the smallest dissipative motions remain unresolved in LES, their effect, represented by the residual stress tensor $\bar{\tau}_{ij}$ on the resolved scales requires proper modeling. Two models are considered in this work: the dynamic Smagorinsky model and the multiscale Smagorinsky model. The dynamic Smagorinsky model for the residual stress tensor is expressed as function of the resolved strain rate tensor $\bar{S}_{ij}$ and the strain rate magnitude $\bar{S}$ as

$$\bar{\tau}_{ij} = -2\nu_e \bar{S}_{ij} = -2C_s^2 \Delta_c^2 \overline{\bar{S}\bar{S}_{ij}}, \tag{69}$$

in which the value of the Smagorinsky constant C_s^2 is determined by the dynamic procedure of Germano et al. [28]. This procedure, which makes use of a secondary filter $\mathcal{G}(\mathbf{x}, \lambda_c)$ with cutoff wavenumber $\lambda_c \leqslant \kappa_c$, guarantees that the magnitude of the subgrid dissipation is adapted appropriately according to the resolved scales in the flow. This implies that the residual stress model is only engaged when the resolution is insufficient to resolve all scales of motion. Moreover, the dynamic procedure is expected to return to the theoretical value $C_s = 0.17$ found by Lilly [29] as soon as the flow is fully turbulent. The second model is the multiscale Smagorinsky model. This model, proposed by Hughes et al. [30,31], relies on an *ab initio* scale separation of the resolved velocity field, by segregating the resolved scales into *large resolved scales* and *small resolved scales*, through an additional projective filtering operator $\mathcal{G}(\mathbf{x}, \lambda_c)$ with cutoff wavenumber $\lambda_c \leqslant \kappa_c$. Hence, the resolved velocity field $\bar{\mathbf{u}}(\mathbf{x}, t)$ can be divided into

$$\bar{\mathbf{u}}(\mathbf{x}, t) = \tilde{\mathbf{u}}(\mathbf{x}, t) + \mathbf{u}''(\mathbf{x}, t), \tag{70}$$

where $\tilde{\mathbf{u}}(\mathbf{x}, t) = \tilde{\bar{\mathbf{u}}}(\mathbf{x}, t)$ indicates the largest resolved scales and $\mathbf{u}''(\mathbf{x}, t)$ denotes the smallest resolved scales, such that

$$\hat{\tilde{\mathbf{u}}}(\boldsymbol{\kappa}, t) = \widehat{\mathcal{G}}(\boldsymbol{\kappa}, \lambda_c)\hat{\bar{\mathbf{u}}}(\boldsymbol{\kappa}, t), \quad 0 \leqslant \kappa \leqslant \lambda_c, \tag{71}$$

$$\hat{\mathbf{u}}''(\boldsymbol{\kappa}, t) = [1 - \widehat{\mathcal{G}}(\boldsymbol{\kappa}, \lambda_c)]\widehat{\mathcal{G}}(\boldsymbol{\kappa}, \kappa_c)\hat{\bar{\mathbf{u}}}(\boldsymbol{\kappa}, t), \quad \lambda_c \leqslant \kappa \leqslant \kappa_c. \tag{72}$$

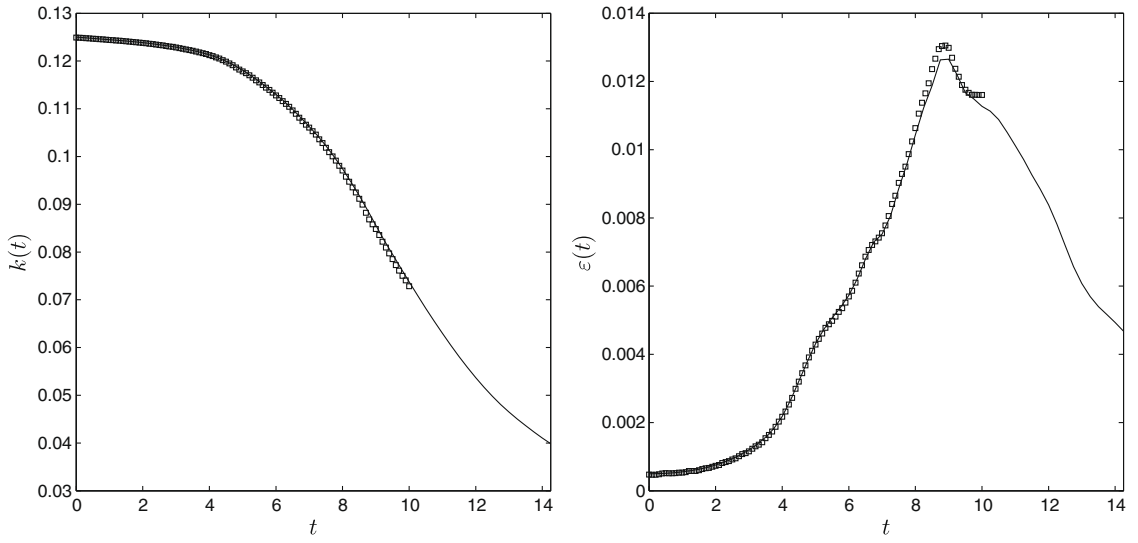

Fig. 8. Direct numerical simulation of Taylor–Green vortex. Temporal evolution of the decaying kinetic energy $k(t)$ (left) and the rate of dissipation $\varepsilon(t)$ (right). (—) DNS results at Re = 1500; (□) DNS of Brachet et al. [14] at Re = 1600. Notice the maximum dissipation at $t = 9$.

Under the assumption that the distant triadic interactions, i.e. interactions between the largest resolved scales $\tilde{\mathbf{u}}$ and the residual scales $\mathbf{u}'$, have a negligible influence on the large scale dynamics, only the contributions of the local triadic interactions between the smallest resolved scales $\mathbf{u}''$ and the residual scales $\mathbf{u}'$ are modeled. Hughes et al. [30,31] proposed to close the residual stress tensor of the small-scale part by an eddy-viscosity model of the Smagorinsky type. In this work the multiscale Smagorinsky model, which is given by

$$\bar{\tau}_{ij} = -2(\nu_e S''_{ij})'' = -2C^2_{s,m}\Delta_c^2(S''S''_{ij})'', \tag{73}$$

will be considered. Note that the total residual stress model is projected again to the small scale velocity field due to the band-pass filter $(\cdot)''$. The model constant C_s is evaluated analogously as done by Lilly [29], although here, both cutoff wavenumbers need to be accounted for. This results into expression

$$C_{s,m} = C_s \frac{\kappa_c}{\lambda_c}\left[\left(\frac{\kappa_c}{\lambda_c}\right)^{4/3} - 1\right]^{-3/4}, \tag{74}$$

for the Smagorinsky coefficient [30]. It can be verified that for $\lambda_c < \kappa_c$, $C_{s,m}$ is larger than the standard Smagorinsky coefficient $C_s \approx 0.17$.

In the present work, the large-eddy simulation of the periodic Taylor–Green vortex flow at Re = 1500($\mathrm{Re}_\lambda \approx 55$) is performed on the uniform computational grid with 64^3 nodes and with grid cutoff wavenumber $\kappa_{max} = \pi/\Delta = 32$. The cutoff wavenumber λ_c that determines the secondary sharp cutoff filter in the dynamic procedure or the sharp cutoff scale-separation filter in the multiscale model is determined as $\lambda_c = \kappa_c/2 = \kappa_{max}/3$. The LES-equations (67) and (68) are solved with the pseudo-spectral method on the one hand and with various finite difference methods, including the dynamic finite difference method on the other hand. Similar to the direct numerical simulation, the skew-symmetric formulation is adopted for the discretization of the nonlinear term, whereas the time stepping is performed again with the explicit low-storage 4-stage Runge–Kutta method with standard coefficients $\left[\frac{1}{4}, \frac{1}{3}, \frac{1}{2}, 1\right]$ and with a time step $\Delta t = 0.005$.[5]

5.3. Implementation of the dynamic finite difference scheme

Before analyzing the results, some particularities must be addressed concerning the implementation of the dynamic finite difference approximations for the large-eddy simulation of the Taylor–Green vortex flow. Indeed, since the spectra related to fields $\overline{u_i}$ and $\overline{u_j}\overline{u_i}$ are substantially different, the value of the dynamic coefficients $c^{dyn}_{k,n}$ in the dynamic finite difference approximations of the advective operator is not the same as the one obtained for the divergence operator. As a consequence, the skew-symmetric formulation of the nonlinear term, constructed by a fixed weighting between the advective and divergence formulation, looses the a priori conservation of kinetic energy [13]. Hence, in order to preserve the skew-symmetry property, and thus the conservation of kinetic energy, the same dynamic coefficient $c^{dyn}_{k,n}$ as obtained for the advective operator is used

[5] Note that the time-step could be increased in case of LES. In this work, however, the same time-step as for the DNS is preferred in order to avoid time-integration ambiguities.

for the divergence operator. Such an approach is equivalent to the traditional discretization approach of the skew-symmetric operator using standard schemes or prefactored optimized schemes.

In the current study, each partial derivative in the Navier–Stokes equations or the Poisson equation is discretized straightforwardly by using the appropriate dynamic finite difference approximation. However, this implementation involves the calculation of multiple dynamic coefficients at each Runge–Kutta step. An overview of all required dynamic coefficients in the system of equation is given below.

1. The finite difference approximation of the nonlinear term in the Navier–Stokes equations requires the calculation of nine dynamic coefficients, i.e. one per component of the skew-symmetric operator.
2. Similarly, three dynamic coefficients are needed for the finite difference approximation of the pressure gradient in the Navier–Stokes equations.
3. Since the molecular viscosity term uses the Laplacian of the velocity field, again nine coefficients must be determined.
4. Although the subgrid force is supposed to sufficiently dissipate the small scales corresponding to high wavenumber Fourier modes, direct evaluation of $\frac{\delta\tau_{ij}}{\delta x_j}$ would result into weak dissipation due to the poor Fourier characteristics of the successive derivative operators. Moreover, spurious π-*modes* at $\kappa = \kappa_{max}$, are not detected by the dissipative operator $\frac{\delta\tau_{ij}}{\delta x_j}$, since the Fourier characteristics vanish for these modes. Hence, they are not eliminated from the solution, unless explicit filtering is used. It is known that these π-*waves* severely pollute the solution and eventually destabilize the algorithm. In order to guarantee the compactness, i.e. minimal stencil width, of the discretization of the subgrid force, it is implemented in this work as

$$\frac{\delta\tau_{ij}}{\delta x_j} = -2\frac{\delta\nu_e}{\delta x_j}\bar{S}_{ij} - 2\nu_e\frac{\delta^2\bar{u}_i}{\delta x_j^2}. \tag{75}$$

   Due to this discretization, three additional dynamic coefficients are required for the partial derivatives of the turbulent viscosity. For the discretization of the Laplacian in expression (75), the same coefficients are used as those obtained for the molecular term.
5. As mentioned earlier, the Pressure-Correction algorithm is used in order to impose the continuity constraint. This algorithm involves the solution of the Poisson equation for the pressure correction. For the construction of the Poisson matrix, the stencils of the Poisson operator must be specified a priori and thus nine values of the dynamic coefficients must be determined in advance. However, since the pressure correction field is not known a priori, these coefficients can only be obtained from the pressure at the previous iteration level.
6. Finally, for the approximation of the divergence operator of predictor velocity u_i^* in the Poisson equation, three dynamic coefficients must be calculated.

The above considerations bring the total amount of required dynamic coefficients per Runge–Kutta step to 36. The optimal blending factors f, used in the dynamic finite difference approximations of the pressure and velocity related terms can be found in Table 1.

The current straightforward implementation of the dynamic finite difference schemes requires the calculation of 36 dynamic coefficients at each Runge–Kutta step, that is 4 times per time step, leading inevitably to a significant computational overhead. It was found for the large-eddy simulation of the Taylor–Green vortex, that the *total computational time* was about 68% higher for the dynamic schemes in comparison with the DRP schemes and the standard schemes. Despite the good performance of the dynamic schemes, which was already demonstrated in Fauconnier et al. [13], an overhead of 68% may be considered prohibitive for practical computations. However, it might sufficient to calculate each dynamic coefficient only once per time step, or even once per few time steps, depending on the time increment Δt and the time scale τ_η of the smallest resolved eddies. Indeed, since the time scale ratio $\theta = \Delta t/\tau_\eta$ must be chosen sufficiently small in order to avoid numerical dissipation, one can expect that the flow physics do not change much during one time step. Hence, evaluating the coefficients each $1/\theta$ time steps, i.e. after one time scale τ_η, should be sufficient. In this work, all 36 dynamic coefficients are evaluated only every 10 time steps. In that case, the computational overhead is only 1.7%. In order to reduce the computational overhead even further, one could think of monitoring only one single dynamic coefficient every few time steps, and adjust the others as soon as the change of the monitored coefficient becomes significant. This is however, not considered in this work.

6. Quantification of numerical errors

Before assessing the quality of the dynamic finite difference approximations in the LES of the Taylor–Green vortex flow, an appropriate and consistent evaluation method must be defined that allows to quantify the different sources of error due to modeling and numerical approximation, and their interactions. In order to separate modeling and numerical errors the *error decomposition method* of Vreman et al. [15] and Meyers et al. [16,32,1] is adopted. Once the error sources are identified by this separation method, a certain *error norm* can be defined which quantifies the magnitude of the respective error sources. The described approach is further discussed in more detail.

Consider the reference solution, obtained by, e.g. direct numerical simulation, which is characterized by the viscous scale κ_η. Further consider a specific flow variable of interest ϕ. Using the same terminology as in [16,32,1], the total error on the

variable of interest ϕ is decomposed into a modeling error contribution and a numerical error contribution, leading to the expressions $\left(\kappa_c = \frac{\pi}{\Delta_c}, \kappa_{max} = \frac{\pi}{\Delta}\right)$

$$\varepsilon_{\phi,total}(\kappa_c,\kappa_{max}) = \overline{\phi_s\left(\kappa_\eta, \frac{3}{2}\kappa_\eta\right)} - \bar{\phi}_{fd}(\kappa_c,\kappa_{max}), \tag{76}$$

$$\varepsilon_{\phi,model}(\kappa_c,\kappa_{max}) = \overline{\phi_s\left(\kappa_\eta, \frac{3}{2}\kappa_\eta\right)} - \bar{\phi}_s(\kappa_c,\kappa_{max}), \tag{77}$$

$$\varepsilon_{\phi,num}(\kappa_c,\kappa_{max}) = \bar{\phi}_s(\kappa_c,\kappa_{max}) - \bar{\phi}_{fd}(\kappa_c,\kappa_{max}), \tag{78}$$

where $\overline{\phi_s\left(\kappa_\eta, \frac{3}{2}\kappa_\eta\right)}$ represents the filtered *spectral* DNS solution, $\bar{\phi}_{fd}(\kappa_c,\kappa_{max})$ represents the *finite difference* LES solution with cutoff κ_c on an LES grid with maximum wavenumber κ_{max} and $\bar{\phi}_s(\kappa_c,\kappa_{max})$ represents the *spectral* LES solution with cutoff wavenumber κ_c and numerical resolution κ_{max} determined by the LES grid. Note that this solution would be equivalent with the finite difference LES-solution on an infinitely fine grid $\bar{\phi}_{fd}(\kappa_c,\kappa_\infty)$. The modeling error $\varepsilon_{\phi,model}$ is related to the adopted subgrid closure, whereas the numerical error $\varepsilon_{\phi,num}$ contains contributions of the aliasing errors as well as discretization errors or finite difference errors. In case proper de-aliasing is applied through explicit filtering of the nonlinear term, the numerical $\varepsilon_{\phi,num}$ reduces exactly to the finite difference discretization errors.

In analogy with the work of Meyers et al. [33], the different errors are then quantified using the *mathematics-based* and *physics-based* error definitions. Two *mathematics-based* error definitions are defined, i.e. the spectrum of the pointwise error ε_ϕ of a variable ϕ

$$E_{\varepsilon_\phi}(\boldsymbol{\kappa},t) = \widehat{\varepsilon_\phi}(\boldsymbol{\kappa},t)\widehat{\varepsilon_\phi}^*(-\boldsymbol{\kappa},t), \tag{79}$$

and its magnitude k_{ε_ϕ}

$$k_{\varepsilon_\phi}(t) = \iiint_{\mathbf{0}}^{\boldsymbol{\kappa}_{max}} E_{\varepsilon_\phi}(\boldsymbol{\kappa},t)d\boldsymbol{\kappa}. \tag{80}$$

Note that the magnitude k_{ε_ϕ} is related to the L_2-norm, as $L_2(t) = (2\pi)^3\sqrt{k_{\varphi}(t)}$ and that this error has always a positive sign.

The *physics-based* error definitions are based on the error of the energy spectrum of the velocity field, which is given by

$$\varepsilon_E(\boldsymbol{\kappa},t) = \Delta E_u(\boldsymbol{\kappa},t) = \Delta[\phi(\boldsymbol{\kappa},t)\phi^*(\boldsymbol{\kappa},t)]. \tag{81}$$

Three global *physics-based* error norms are then introduced, i.e. the total error on the longitudinal integral length scale L_{11}, the total error on the kinetic energy k, and the total error on the dissipation rate ε, given by respectively

$$\varepsilon_L(t) = \Delta L_{11} = \iiint_{\mathbf{0}}^{\boldsymbol{\kappa}_{max}} \boldsymbol{\kappa}^{-1}\Delta E_u(\boldsymbol{\kappa},t)d\boldsymbol{\kappa}, \tag{82}$$

$$\varepsilon_k(t) = \Delta k = \iiint_{\mathbf{0}}^{\boldsymbol{\kappa}_{max}} \Delta E_u(\boldsymbol{\kappa},t)d\boldsymbol{\kappa}, \tag{83}$$

$$\varepsilon_\varepsilon(t) = \Delta\varepsilon = \iiint_{\mathbf{0}}^{\boldsymbol{\kappa}_{max}} \boldsymbol{\kappa}^2\Delta E_u(\boldsymbol{\kappa},t)d\boldsymbol{\kappa}. \tag{84}$$

Remark that the sign of ε_k and ε_ε could be either positive or negative, enabling to see interactions between different error sources. Time-integration of these time-dependent error norms results in a single-value error norm. Following Meyers et al. [33], this norm is defined as

$$\delta_\phi = \left\{ \frac{\int_0^{t_{max}} \left[\iiint_{\mathbf{0}}^{\boldsymbol{\kappa}_{max}} \boldsymbol{\kappa}^q (E_{u,ref}(\boldsymbol{\kappa},t) - E_u(\boldsymbol{\kappa},t))d\boldsymbol{\kappa}\right]^2 dt}{\int_0^{t_{max}} [\boldsymbol{\kappa}^q E_{u,ref}(\boldsymbol{\kappa},t)d\boldsymbol{\kappa}]^2 dt} \right\}^{1/2} \tag{85}$$

in which the parameter $q = -1, 0, 2$ determines the specific physics-related quantity ϕ, i.e. L_{11}, k or ε. The reference spectrum $E_{u,ref}(\boldsymbol{\kappa},t)$ can either be that of the spectral LES in case of numerical errors, or that of the DNS in case of modeling errors and total errors.

It is emphasized that the mathematics-based error definitions reflect both amplitude and phase errors in the solution whereas the physics-based definitions represent only errors on the amplitude. Both error definitions are used further for analyzing the performance of finite difference schemes, and interactions with the subgrid model.

7. Numerical results

7.1. Modeling error contributions

Before assessing the quality of the dynamic finite difference scheme, the modeling errors related to the dynamic Smagorinsky model and the multiscale model are briefly discussed. As mentioned before, the modeling error contributions and the

numerical error contributions are separated by the decomposition of Vreman et al. [15] and Meyers et al. [16,32,1]. Fig. 9 shows the decay of resolved kinetic energy k_r and the relative percentage of resolved kinetic energy for the filtered DNS solution and the spectral LES solutions with the dynamic Smagorinsky model and the multiscale Smagorinsky model. For homogeneous isotropic turbulence, the kinetic energy decays according to the power law $k \sim t^{-n}$. The decay exponents for the DNS and LES simulations of the Taylor–Green vortex are found to lie in between $n = 1.3$, which is generally accepted as the decay exponent at high Reynolds numbers, and $n = 2.5$, which is the decay exponent in the final period of decay where the viscous effects become dominant. This result indicates that the Reynolds number is rather low such that viscous effects are not negligible. According to Pope [35], about 80% of the kinetic energy should be resolved in order to have a good large-eddy simulation. Although the filtered DNS solution indicates that at least 98% of the kinetic energy may ideally be resolved on the 64^3 LES-grid, both spectral LES solution resolve less kinetic energy. Using the dynamic Smagorinsky model, only 78% of the kinetic energy is resolved at the end of the simulation, despite the use of a dynamic procedure. Indeed, it was verified that the predicted dynamic coefficient C_s, which is zero at the beginning of the simulation, remains substantially below the theoretical value $C_s = 0.17$ obtained by Lilly [29] when the flow is fully turbulent. On the other hand, the multiscale model performs better and at the end of the simulation, the resolved kinetic energy decreases to about 85%.

Fig. 10 displays the resolved dissipation rate ε_r, accentuating the modeling error on the smallest resolved scales, and the total dissipation rate ε_{tot} which contains resolved and subgrid contributions. The results show that the multiscale model performs better than the dynamic Smagorinsky model. However, the total dissipation rate ε_{tot} and the resolved kinetic energy k_r indicate that the underlying eddy-viscosity model is too dissipative, despite the use of a multiscale technique or a dynamic procedure. Indeed, both modeling techniques lead to an overestimation of the turbulent dissipation in the early transitional stages ($t \leqslant 6$), and although the prediction of the dissipation is much better in the turbulent stages, the loss of kinetic energy in the early transitional stages cannot be recuperated. In the past decades, many new subgrid modeling approaches were therefore developed. In some of them, the subgrid scales are modeled directly for the primitive variables in the LES equations. Such methods rely on the reconstruction of scales in the velocity field, e.g. by means of a deconvolution procedure [36]. A more comprehensive review is given by Domaradzki and Adams [37]. Such methods are claimed to be less dissipative than the basic eddy viscosity models and therefore advantageous for application in large-eddy simulation. One of these techniques is the adaptive local deconvolution method (ALDM) of Hickel et al. [34]. This method involves a solution-adapted deconvolution operator that controls the (dissipative) truncation error in the framework of implicit LES and the deconvolution parameters within the method are selected by analysis of the spectral numerical viscosity. This new approach, which was claimed to perform at least as well as the established models, was successfully applied to the large-eddy simulation of the Taylor–Green vortex at $\mathrm{Re} = 1600$ [34] on a 64^3-grid. Despite the small difference in Reynolds number, the ALDM-results may be compared to the results in the current study. Fig. 10 shows reasonable good agreement between the resolved and total dissipation rates obtained by the Smagorinsky models and that of the ALDM method. However, whereas the resolved dissipation for the eddy-viscosity models is slightly too high in the pre-transitional zone ($4 \leqslant t \leqslant 7$), leading to a reduction in resolved kinetic energy, the resolved dissipation for the ALDM method is slightly too low there, leading to an increased resolved kinetic energy. Nevertheless, Fig. 9, right, clearly shows that the modeling errors of both eddy-viscosity models and the ALDM method have comparable magnitudes, but different signs. This leads us to conclude that the results obtained with both eddy viscosity models are certainly acceptable, and that the modeling errors are comparable to those in

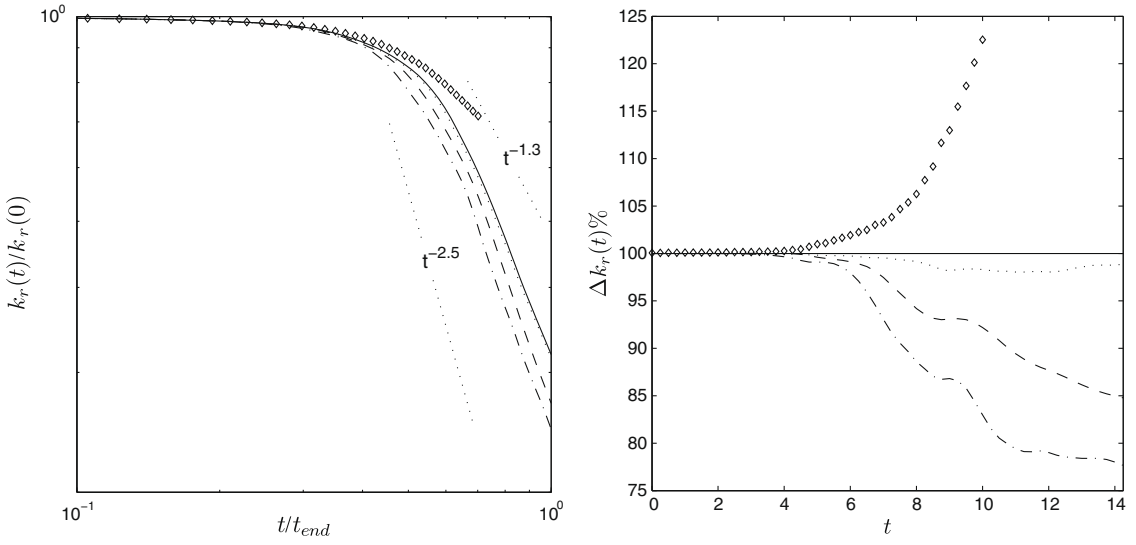

Fig. 9. Temporal decay of resolved kinetic energy (left) and Percentage of resolved kinetic energy $\Delta k_r(t)\%$ (right). Distinguish the DNS solution (—), the filtered DNS solution (···) and the spectral LES solutions obtained with the dynamic Smagorinsky model (-·-·-), the multiscale model (– – –) and the ALDM results of Hickel et al. [34] (◇).

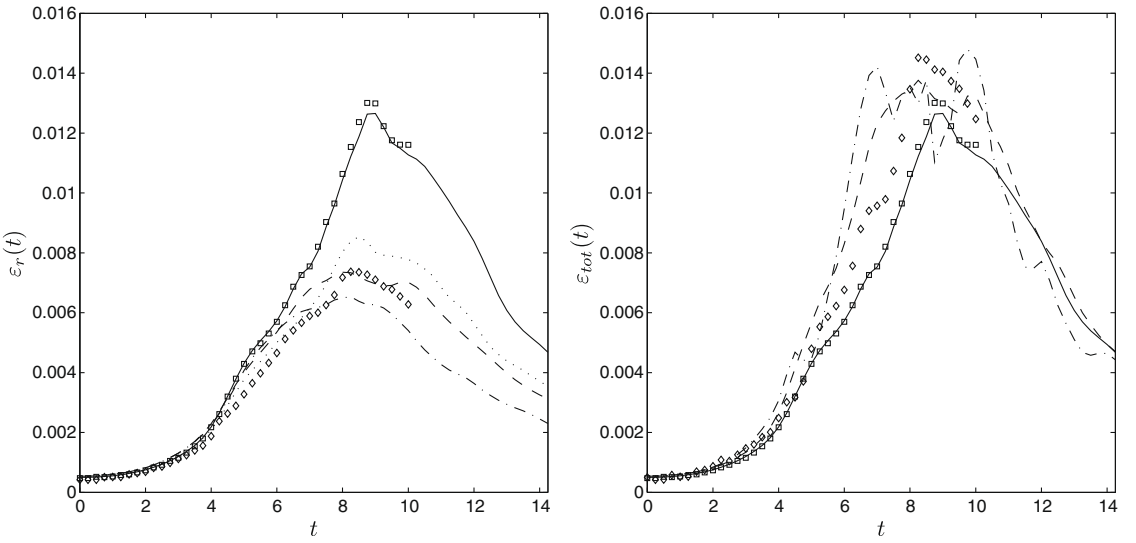

Fig. 10. Resolved dissipation $\varepsilon_r(t)$ (left) and total dissipation (resolved + subgrid) $\varepsilon_{tot}(t)$ (right). Distinguish the DNS solution (−), the DNS of Brachet et al. [14] (□), the filtered DNS solution (· · ·) and the spectral LES solutions obtained with the dynamic Smagorinsky model (-·-·-), the multiscale model (– – –) and the ALDM results of Hickel et al. [34] (◇).

other types of large-eddy simulations with non-eddy-viscosity models. In the following error-assessment, the multiscale model is considered to be better than the dynamic model, due to the smaller modeling errors. Fig. 11 displays a snapshot of the energy spectra at time $t = 7$, i.e. when the flow is going into transition and at time $t = 14$ when the fully developed turbulence is decaying. It is seen that the dynamic Smagorinsky model is too dissipative in the entire wavenumber range. In contrast, the multiscale model leads to a slight energy pile-up around the scale separation cutoff wavenumber $(\kappa_{max}/3)$, e.g. at $t = 14$. Although a significant reduction of subgrid dissipation on the smallest resolved scales is seen, we also observe a slightly increased dissipation on the largest resolved scales. This is rather surprising, since the multiscale model does only dissipate in the high wavenumber region $\left[\frac{\kappa_{max}}{3}, \frac{2\kappa_{max}}{3}\right]$. Although the precise reason for this phenomenon remains somewhat unclear at the moment, it is not essential for the further discussion.

7.2. Mathematics-based numerical error contributions

The quality assessment of the dynamic finite difference approximations is initiated by comparing the numerical errors with those of the standard schemes and DRP schemes. Fig. 12 displays the global magnitude of the numerical errors (related to L_2-norm) on the resolved velocity field $\bar{\mathbf{u}}(\mathbf{x}, t)$, obtained from the large-eddy simulation with the dynamic Smagorinsky model. Analogous results were obtained with the multiscale model. Since the error profiles on the pressure field $p(\mathbf{x}, t)$ are again very similar for both models, they are not shown here. It is observed that the dynamic schemes recover the asymptotic order of accuracy in the early stages of the simulation, i.e $t \leqslant 2$, where the flow is still smooth and resolved with DNS-resolution. This is in contrast to the Dispersion-Relation Preserving schemes, which are suboptimal in these situations, since they have an a priori optimization to a fully developed uniform spectrum. As soon as the resolution of the computational grid becomes inadequate to resolve all scales in the flow (the simulation shifts from DNS-resolution to LES-resolution at $t \approx 2$), the dynamic schemes adapt to the instantaneous solution and achieve an accuracy which is at least as good, or better than that of the Dispersion-Relation Preserving schemes at all times $2 \leqslant t \leqslant 14.25$. It is emphasized that the dynamic schemes switch form higher-order accuracy to DRP-mode as soon as the smallest resolved scales, which are marginally resolved, become important in the flow, even when the flow is still laminar at that time. Indeed, although the energy spectrum of a laminar flow may not be characterized by an inertial range as for a turbulent flow, it still contains a spectrum of scales which must be resolved accurately, and since the value of the dynamic coefficients is correlated to the energy spectrum, the scheme adapts even in case of laminar flows. This indicates that the dynamic schemes respond to both the mean flow phenomena and turbulence. Studying the results in more detail, the 2nd-order explicit dynamic scheme is observed to achieve the accuracy of the 8th-order central scheme, which is better than that of the corresponding 2nd-order DRP scheme. The latter has a comparable accuracy to that of the standard 6th-order explicit scheme. The 4th-order explicit dynamic scheme obtains slightly better quality than the corresponding DRP scheme, which fluctuates between that of the 8th- and 10th-order standard scheme, although the difference becomes very small. Further the performance of the 4th-order dynamic implicit finite difference approximation almost collapses with that of the 4th-order implicit Padé scheme and both clearly outperform all other schemes, including the standard tridiagonal Padé scheme. For a fully developed inertial range spectrum the difference in accuracy between the dynamic finite difference approximations and the DRP schemes decreases with increasing order of

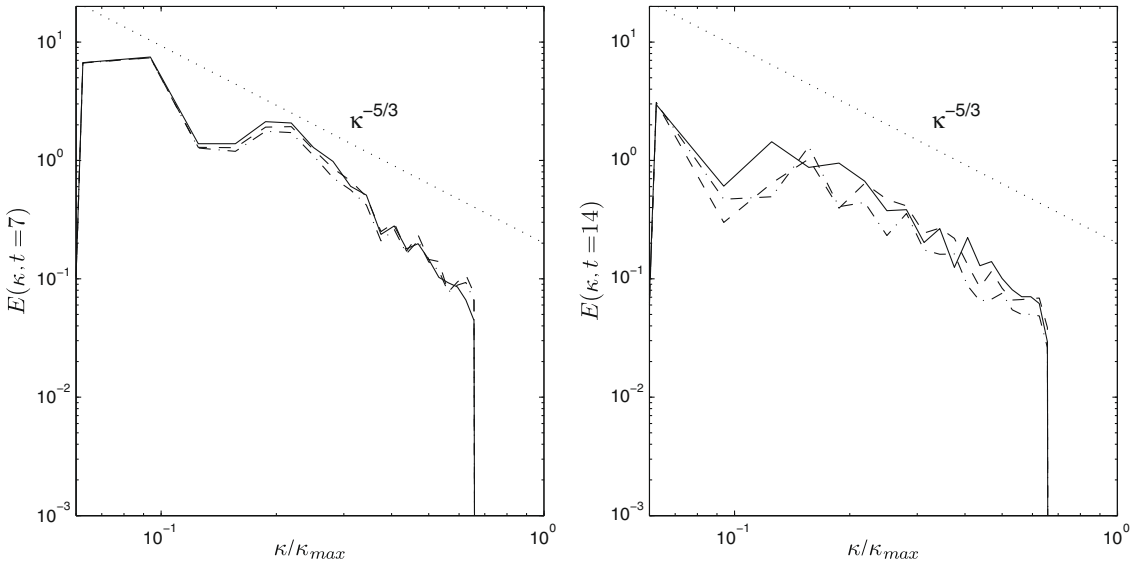

Fig. 11. The energy spectra of the filtered DNS results (—), the pseudo-spectral LES results with dynamic Smagorinsky (-·-·) and with the multiscale Smagorinsky (---) at time $t = 7$ (left), i.e. when the flows develops into turbulence and at $t = 14.00$, i.e. when the turbulence is decaying (right).

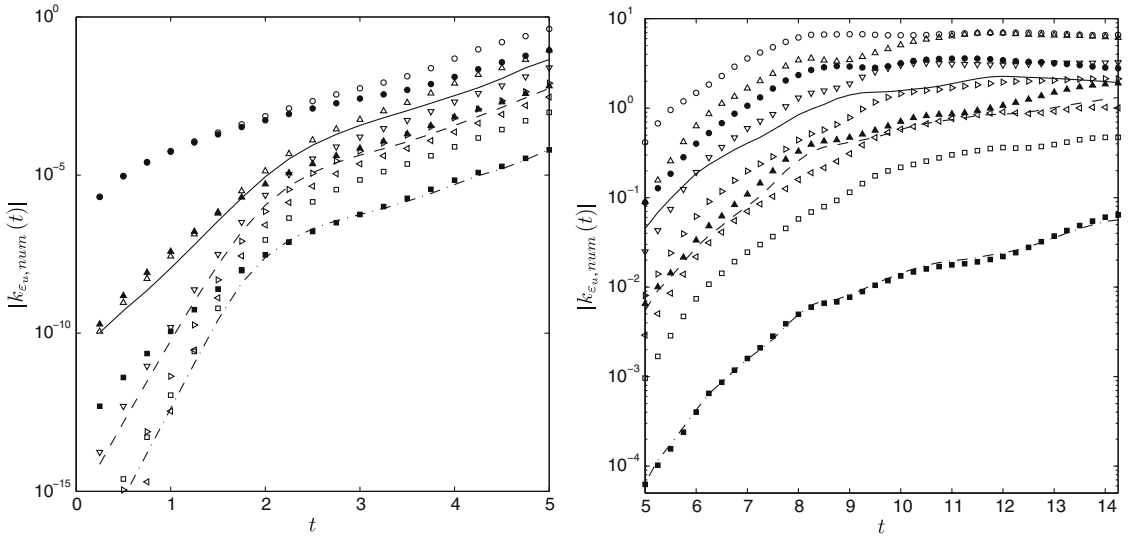

Fig. 12. The global magnitude $k_{\varepsilon_{u,num}}$ of the numerical errors on the resolved velocity field $\bar{\mathbf{u}}(\mathbf{x}, t)$, obtained from the large-eddy simulation of the Taylor–Green vortex with the dynamic Smagorinsky model: the laminar stages of the Taylor–Green flow at times $0 \leqslant t \leqslant 5$ (left) and the transitional and turbulent stages at times $5 \leqslant t \leqslant 14.25$ (**right**). (○) 2nd-order; (△) 4th-order; (▽) 6th-order; (▷) 8th-order; (◁) 10th-order; (□) 6th-order Padé; (•) 2nd-order explicit DRP; (▲) 4th-order explicit DRP; (■) 4th-order DRP Padé; (—) 2nd-order explicit dynamic; (– – –) 4th-order explicit dynamic; (-·-·) 4th-order dynamic Padé.

accuracy of the underlying finite difference approximation. This also shows that the importance of the inertial range slope β in calibration procedure for the dynamic schemes at $\mathrm{Re} \to \infty$ decreases quite fast for higher-order dynamic schemes. This is in agreement with the observations in Figs. 4–6. Further, it is noticed that the dynamic schemes and the DRP schemes lead to a significant gain in numerical accuracy in comparison with the standard schemes. This conclusion supports the observations of Berland et al. [5]. Fig. 13 illustrates the more detailed energy spectrum of the numerical errors at the early stages of the simulation ($t = 1$) and when the flow is fully turbulent ($t = 9$). One can see that in the early stages of the simulation ($t = 1$), the dynamic schemes are clearly adapted to the low-wavenumber content on the computational grid, whereas for the fully developed turbulent flow ($t = 9$), the dynamic schemes are optimized for the inertial range turbulent spectrum. The results above demonstrate already the ability of the dynamic finite difference schemes to adapt to the changes in the energy spectrum or to changes in the filter-to-grid cutoff ratio κ_c/κ_{max}.

To illustrate further the adaptivity of the dynamic schemes, Fig. 14 shows the various ratios of the dynamic coefficient to its Taylor value $c^{dyn}_{k,n}/c^{*}_{k,n}$, for the 4th-order explicit dynamic finite difference approximation of the skew-symmetric operator

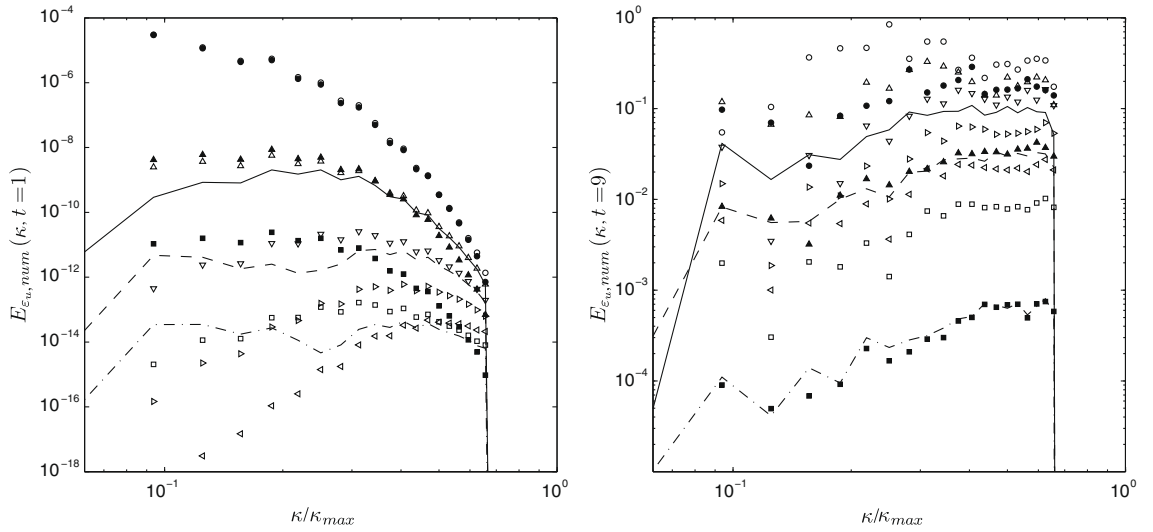

Fig. 13. Snapshots of the spectrum $E_{\varepsilon_u}(\kappa,t)$ of the error of the resolved velocity field of the laminar Taylor–Green vortex flow at $t=1$ (left) and the fully turbulent Taylor-Green flow at $t=9$ (right). (○) 2nd-, (△) 4th-, (▽) 6th-, (▷) 8th- and (◁) 10th-order standard schemes; (□) 6th-order Padé; (●) 2nd- and (▲) 4th-order explicit DRP schemes; (■) 4th-order DRP Padé; (—) 2nd- and (– – –) 4th-order explicit dynamic schemes; (-·-·-) 4th-order dynamic Padé.

$\frac{1}{2}u_j\frac{\partial u_i}{\partial x_j}+\frac{1}{2}\frac{\partial u_j u_i}{\partial x_j}$, as function of time. Remark that due to the symmetries of the flow, some of the obtained dynamic coefficients for the different contributions of the skew-symmetric operator $\frac{1}{2}u_j\frac{\partial u_i}{\partial x_j}+\frac{1}{2}\frac{\partial u_j u_i}{\partial x_j}$ are equal, more specifically components $(i,j)=(1,1)=(2,2),(1,2)=(2,1),(1,3)=(2,3)$ and $(3,1)=(3,2)$ are equal. Therefore, these dynamic coefficients are not explicitly shown in Fig. 14. First, the scheme recovers the asymptotic order of accuracy at the initial stages of the simulation, since $c_{k,n}^{dyn}/c_{k,n}^{*}\to 1$. Further, a sharp increase of the coefficient is observed around $1\leqslant t\leqslant 2$. This stems from the fact that the simulation shifts around that time from DNS-resolution to LES-resolution, although the flow is still laminar. Notice that the coefficients of the different contributions increase independently from each other, due to the anisotropy of the initial Taylor–Green vortex flow. This clearly illustrates the behaviour of the dynamic schemes to smoothly adapt according to the specific properties of the flow on the computational grid, including global anisotropy. Hence, such schemes might provide an additional advantage for accurate simulations of more complex anisotropic flows. In the interval $5\leqslant t\leqslant 8$, where the flow goes into transition, the dynamic coefficients seem to reach an intermediate plateau. Once the coherent structures break down ($t\approx 8$), the dynamic coefficients $c_{k,n}^{dyn}$ increase slightly and approach the theoretical value found in Table 1.

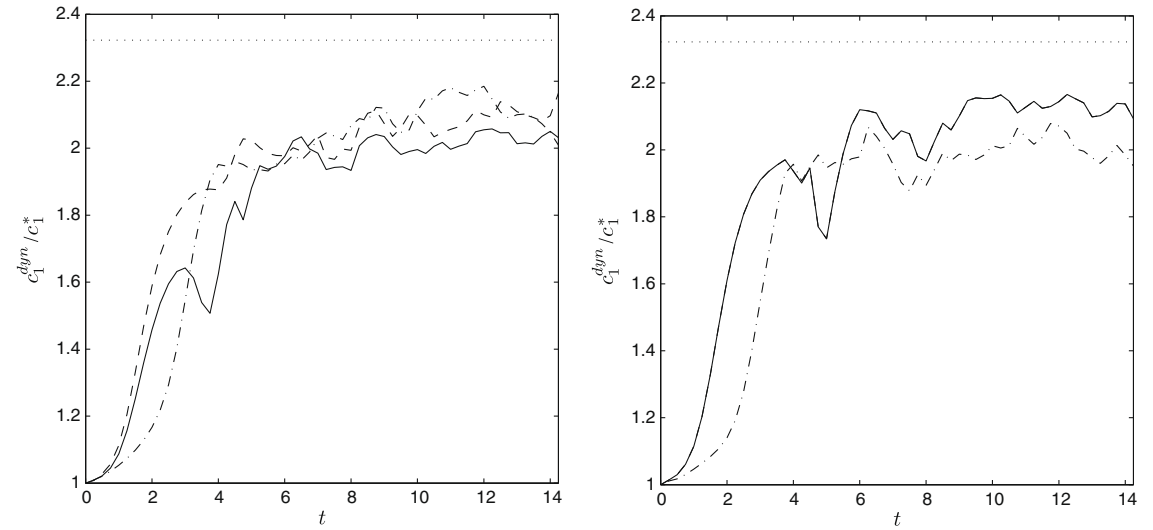

Fig. 14. Ratio of the dynamic coefficient to its Taylor value $c_{k,n}^{dyn}/c_{k,n}^{*}=c_n^{dyn}/c_n^{*}$ for the 4th-order explicit dynamic approximation of the skew-symmetric disretizaton of the nonlinear term, i.e. $\frac{1}{2}u_j\frac{\partial u_i}{\partial x_j}+\frac{1}{2}\frac{\partial u_j u_i}{\partial x_j}$. The coefficients for $i=1$ (left) and $i=3$ (right) with $j=1$ (—), $j=2$ (– – –) and $j=3$ (-·-·-) are illustrated. The optimized coefficient (Table 1) for the corresponding 4th-order Dispersion-Relation Preserving scheme, is shown for comparison (···).

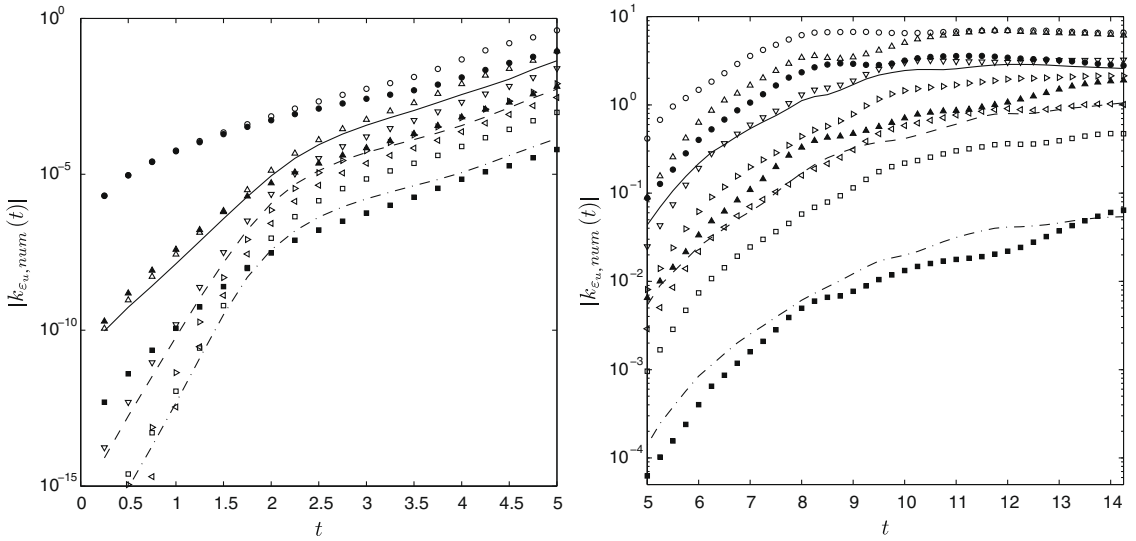

Fig. 15. The global magnitude $k_{\varepsilon_u,num}$ of the numerical errors on the resolved velocity field $\bar{\mathbf{u}}(\mathbf{x},t)$, obtained from the large-eddy simulation of the Taylor–Green vortex with the dynamic Smagorinsky model: $0 \leqslant t \leqslant 5$ (left) and $5 \leqslant t \leqslant 14.25$ (right). The influence of a suboptimal value for f, in this case $f = f^*$, remains quite small. (○) 2nd-, (△) 4th-, (▽) 6th-, (▷) 8th- and (◁) 10th-order standard schemes; (□) 6th-order Padé; (•) 2nd- and (▲) 4th-order explicit DRP schemes; (■) 4th-order DRP Padé; (—) 2nd- and (– – –) 4th-order explicit dynamic schemes; (-·-·-) 4th-order dynamic Padé.

In order to investigate the sensitivity of the constructed dynamic finite difference schemes to the value of the blending factor f, the large-eddy simulations with the dynamic Smagorinsky model and the dynamic finite difference schemes were repeated, but now with the asymptotic value of the blending factor, i.e. $f^* = f(\kappa_c = 0)$, instead of the optimized value $f(\kappa_c = \frac{2}{3}\kappa_{max})$ (see Fig. 2). Fig. 15 shows the numerical errors of the 2nd- and 4th-order explicit dynamic schemes and of the 4th-order dynamic tridiagonal Padé scheme, each one with the asymptotic value of the blending factor, i.e. $f^* = f(\kappa_c = 0)$. A certain sensitivity of the dynamic schemes to suboptimal values of the blending factor f is noticed. However the penalization on the accuracy due to this suboptimal choice is small. Indeed, the sensitivity is very small for the low-order dynamic schemes, but increases if the basic order increases. The largest penalization in accuracy is observed for the 4th-order tridiagonal dynamic Padé scheme. Nevertheless, the accuracy improvement in comparison with the standard 6th-order tridiagonal Padé scheme is still very large. One can conclude, that the exact value of the blending factor is not crucial for the success of the dynamic schemes, and even suboptimal values can be used safely.

7.3. Physics-based numerical errors and their interaction with the modeling errors

In the previous discussion, the mathematics-based error definitions were used to quantify the numerical errors of the various finite difference schemes. In the following, the physics-based error definitions will be used to evaluate the various finite difference schemes. The impact of the numerics on the longitudinal integral length scale $L_{11}(t)$ and the kinetic energy $k(t)$ is demonstrated in Fig. 16 for the large-eddy simulation of the Taylor–Green vortex with both the dynamic and multiscale Smagorinsky model. Results on the dissipation rate $\varepsilon(t)$ are very similar. Further, results are only shown for the turbulent period of the flow at $7 \leqslant t \leqslant 14.25$, since at earlier times the dynamic finite difference schemes, which are investigated in this work, reduce again to their asymptotic counterparts. Hence the behaviour of the dynamic schemes in the early stages is no different from that in previous discussion despite the different error measures. It is understood from definitions (82)–(84) that, e.g. the error on the longitudinal integral length scale contains more information on the accuracy of the amplitude of the largest resolved scales, whereas the error on the dissipation rate contains more information on the accuracy of the amplitudes of the smallest resolved scales. Hence, accuracy analysis of the parameters $L_{11}(t)$, $k(t)$ and $\varepsilon(t)$ accentuates the numerical accuracy of the various finite difference schemes in a certain spectral band of the wavenumber range. First consider the numerical errors on the longitudinal integral length scale L_{11} and on the kinetic energy k. It is observed that the numerical errors of the standard asymptotic finite difference schemes are negative, which indicates a significant reduction in the dissipation due to the numerics. In contrast, the numerical errors related to the dynamic finite difference schemes and the Dispersion Relation Preserving schemes, remain positive during the simulation, indicating an increased dissipation due to the numerics. However, the magnitudes of the errors are significantly smaller for the dynamic and DRP schemes than for the standard schemes. Adapting the finite difference schemes for the smallest resolved scales such that global dispersion error is minimized remain therefore advantageous since it has a positive effect on the evolution of the largest resolved scales in the flow (as reflected by L_{11}). Hence, the general conclusions that applied to the mathematics-based errors remain valid for the physics-based errors. Further, Fig. 16 indicates that the dynamic finite difference schemes generally perform better than

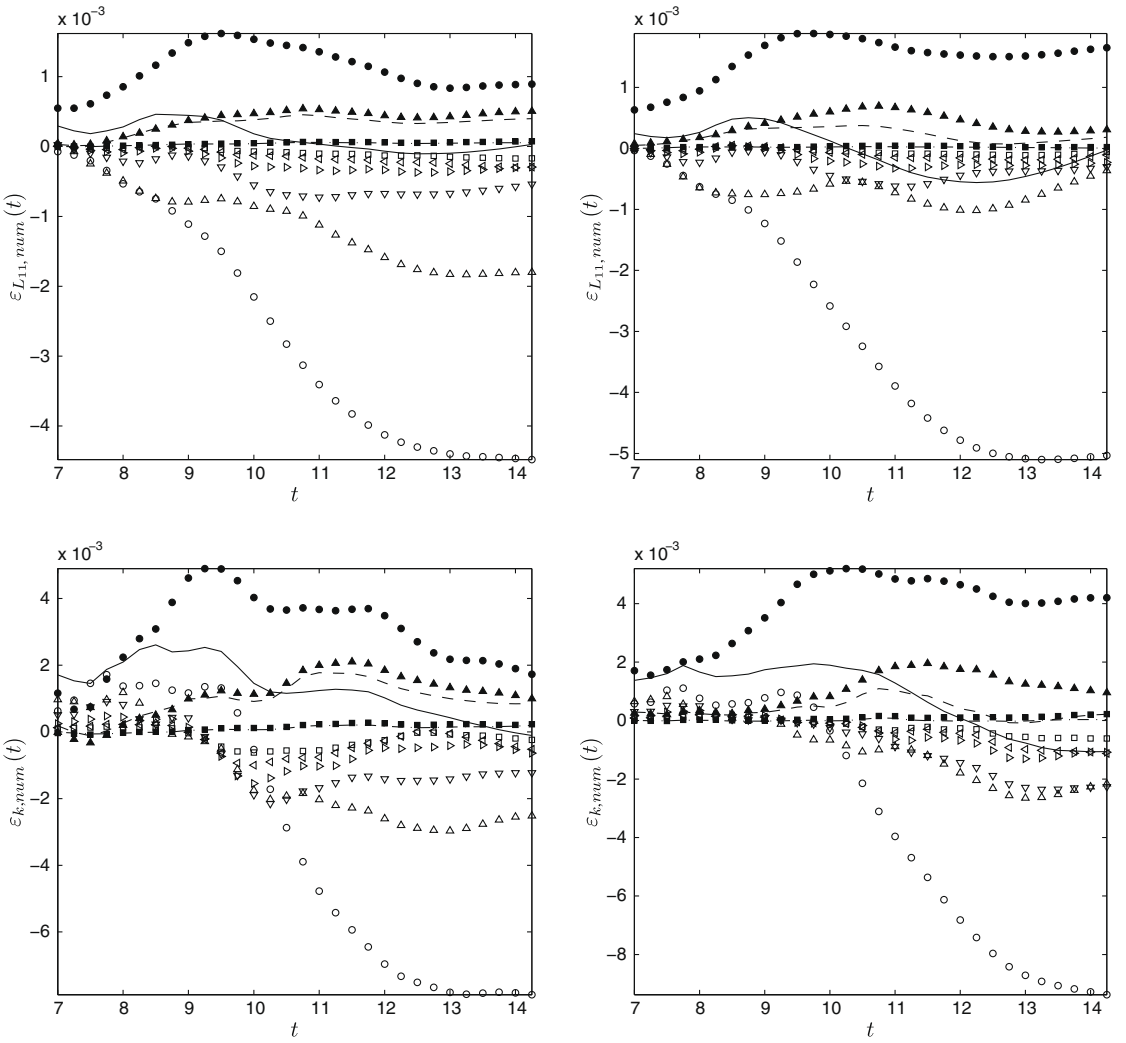

Fig. 16. Numerical errors on the longitudinal integral length scale L_{11} (upper) and the kinetic energy k (lower), in the LES of the turbulent Taylor–Green flow at $7 \leqslant t \leqslant 14.25$: dynamic Smagorinksy model (left) and multiscale Smagorinksy model (right). (○) 2nd-, (△) 4th-, (▽) 6th-, (▷) 8th- and (◁) 10th-order standard schemes; (□) 6th-order Padé; (●) 2nd- and (▲) 4th-order explicit DRP schemes; (■) 4th-order DRP Padé; (—) 2nd- and (– – –) 4th-order explicit dynamic schemes; (-·-·-) 4th-order dynamic Padé.

their Dispersion-Relation Preserving counterparts. For example, this is most obvious for the 2nd-order explicit dynamic scheme in the error-plots of the integral length scale and the kinetic energy. This good performance is mainly attributed to the ability of the dynamic schemes to adapt to changing flow conditions and anisotropy and to the high-Reynolds calibration of the dynamic schemes with the $-5/3$ and $-7/3$ inertial range spectra instead of the uniform spectrum. Finally, the numerical errors obtained with the dynamic model are in the same order of magnitude as those of obtained with the multiscale Smagorinsky model, and the tendencies look quite similar.

Although in the previous discussion a clear numerical improvement is shown for more accurate finite difference errors, this does not indicate whether a better numerical approximation of the model will lead to a better overall performance. Therefore, the total numerical errors are investigated, that is the combination of the numerical errors and the modeling errors on the physics-related quantities. The total errors on the kinetic energy for the large-eddy simulation of the Taylor–Green flow with the dynamic Smagorinsky model ($t \geqslant 7$) are shown in Fig. 17. The total errors on the longitudinal length scale and the dissipation rate are very similar. Fig. 18 depicts the time-integrated numerical and total error norms of the physics-related quantities L_{11}, k, ε for the large-eddy simulations with both the dynamic and multiscale model. In accordance with the results of Meyers et al. [16,32], contingent cancellation of numerical errors and modeling errors are witnessed. These cancellations depend on the specific quantity which is examined. For instance, it is seen that the 2nd-order standard scheme leads to the smallest total errors for the kinetic energy, whereas the 4th-order standard scheme leads to the smallest total errors and the 2nd-order scheme leads to the largest total errors on the longitudinal integral length scale. On the other hand, the 6th-order standard scheme gives the smallest total error on the dissipation rate. In contrast, the higher-order stan-

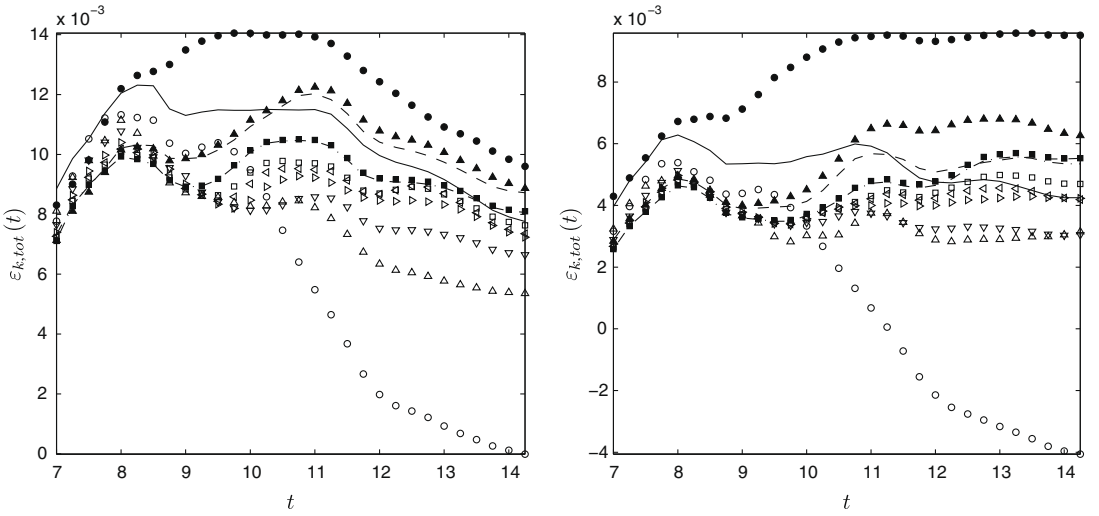

Fig. 17. Total errors on the kinetic energy k, in the large-eddy simulation of the Taylor–Green vortex flow with the dynamic Smagorinsky (left) and the multiscale Smagorinsky model (right) model at $t \geqslant 7$. (○) 2nd-, (△) 4th-, (▽) 6th-, (▷) 8th- and (◁) 10th-order standard schemes; (□) 6th-order Padé; (●) 2nd- and (▲) 4th-order explicit DRP schemes; (■) 4th-order DRP Padé; (—) 2nd- and (– – –) 4th-order explicit dynamic schemes; (-·-·) 4th-order dynamic Padé.

dard schemes, the Dispersion-Relation Preserving schemes and the dynamic finite difference schemes, which are believed to have better spectral characteristics, do not perform as well. For instance, the 2nd-order Dispersion-Relation Preserving scheme leads to the largest total errors on L_{11} and k. Also the 2nd-order dynamic scheme leads to larger total errors in comparison with the high-order standard schemes although they are lower than those of the DRP scheme. In general, the DRP-schemes and the dynamic schemes lead to larger total errors than the standard schemes on L_{11} and k, whereas the standard schemes perform worse on ε. Hence, aside from the observation that better numerical accuracy does not lead automatically to better overall accuracy one may conclude that the best discretization scheme, which gives the lowest the total errors, depends on the investigated quantity. It was verified that the reason for this peculiar behavior must be attributed to the resolution efficiency of the discretization of the viscous terms and the subgrid force. Indeed, low order discretizations of these terms (e.g. 2nd-order standard discretization) implies significant dispersion errors leading to less effective dissipation of the viscous term and the subgrid term. Since eddy-viscosity models were seen to be over-dissipative, the lack of dissipation due to the poor numerics seems advantageous and leads to a better general performance. Hence, improving the numerical efficiency of the finite difference scheme, and thus decreasing the dispersion errors, does not lead to better overall accuracy since it enhances the dissipation. This phenomenon is illustrated in Fig. 19, where the energy spectra of the filtered DNS results, the pseudo-spectral LES results and the 2nd-order finite difference LES results for the multiscale model are shown at times $t = 6$ and $t = 14$. The results with the dynamic Smagorinsky model are similar. Observe that the increased energy pile-up of the 2nd-order solution at the end of the energy spectrum in comparison with the pseudo-spectral solution is due to the reduced dissipation-effectiveness of the numerical method. As a consequence, the drain of energy in the cascade is reduced and the resolved kinetic energy increases.

Nevertheless, Fig. 18 demonstrates that the multiscale model leads to smaller total errors than the dynamic model due to its smaller modeling error contribution. This automatically raises the question if application of an even better subgrid model would give better overall accuracy in combination with more accurate numerical methods. This statement is self-evident in case of a *perfect* subgrid model in which modeling errors were absent. The total error then reduces to the numerical error which decreases with increasing accuracy of the numerical method (see Fig. 18, left). However, since the modeling error with the multiscale model is smaller than with the dynamic Smagorinsky model, the main trend is already visible from the results, though rather subtle. Indeed, comparison of the total errors of the 2nd- and 4th-order standard schemes for both models, demonstrates that the relative gain in accuracy when going from 2nd- to 4th-order is larger for the multiscale model than for the dynamic model. This is most obvious for the longitudinal length scale L_{11}, where the total error of the 2nd-order scheme increases when the modeling error decreases whereas the total error of the 4th-order scheme decreases with decreasing modeling error. Fig. 20 further illustrates this principle by showing the time-integrated total error on the kinetic energy, in which the modeling error contribution is artificially decreased with 0%, 25%, 50%, 75% and 100%, under the assumption that the numerical error remains unaltered. This idealized representation shows clearly that the mean error level decreases with decreasing modeling error, and that the optimal finite difference method, which leads to the lowest total errors, increases in *numerical* accuracy with decreasing modeling error. In conclusion, better subgrid models require more accurate numerical methods in order to minimize the total error. Finally, it is emphasized that in case of the dynamic and multiscale Smagorinsky model, the modeling error and numerical errors of the standard schemes cancel out each other, since they have opposite signs, whereas the modeling errors and the numerical errors of the optimized schemes reinforce

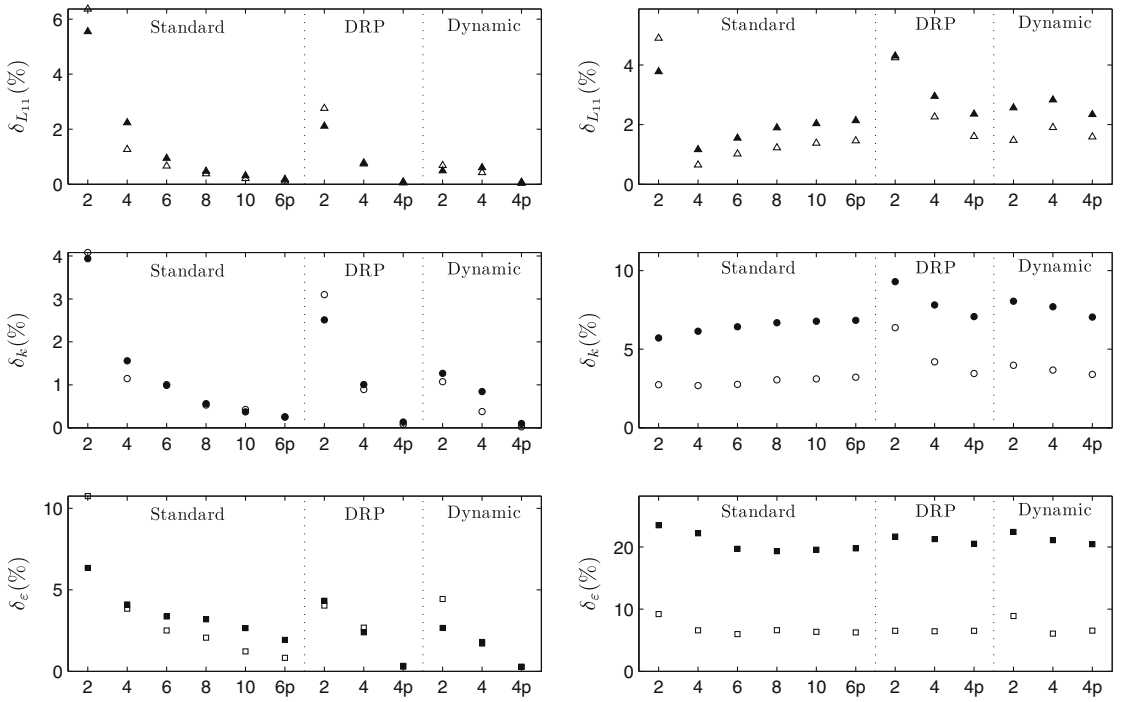

Fig. 18. Time-integrated numerical error norms (left) and total error norms (right) for the different finite difference schemes indicated by their order of accuracy (note that *p* indicates a Padé scheme.). Results are shown for the dynamic Smagorinsky model (▲, ●, ■) and for the multiscale Smagorinsky model (△, ○, □).

each other leading to larger total errors. However, in case of less dissipative non-eddy viscosity methods, using for instance deconvolution operators [36], it may occur that modeling errors have opposite signs than those of eddy-viscosity models (analogous to the situation in Fig. 9). As a consequence, the modeling errors and numerical errors of the standard schemes would probably reinforce each other in such a case, whereas the modeling errors would cancel out the numerical errors related to the optimized schemes. Hence, cancellation of different errors depends not only on the type of numerical schemes, but also on the type of subgrid model.

8. Future perspectives towards general flows

Although the dynamic finite difference schemes are examined in this work for the periodic Taylor–Green vortex flow, they can be applied safely to more complex wall-bounded flows. Indeed, in earlier work of Fauconnier et al. [38,39] the dynamic finite differencing technique was already successfully investigated for the laminar flow in a two-dimensional lid-driven cavity. This study demonstrated that the dynamic finite difference technique allows to increase the numerical accuracy of a wall-bounded laminar flow, by adapting the dynamic coefficients in the discretization scheme according to the specific flow solution. These results in combination with those of the present study, indicate that the value of the dynamic coefficients, which are calculated in physical space using expression (26), does not only depend on the presence of turbulent fluctuations in the flow field, but also on the mean flow characteristics. Since both the mean flow and the turbulent fluctuations contribute to the shape of the energy spectrum, the dynamic coefficients are directly related to the shape of the energy spectrum, which can represent either laminar or turbulent flows.

An issue, closely related to this one, is the behaviour of the dynamic schemes in case of transitional spatially developing flows. In the current investigation of the temporal transitional Taylor–Green vortex flow, a global averaging is assumed in the least-squares approximation (26) for the dynamic coefficients. In case of transitional spatially developing flows, one might consider to use a local averaging instead of a global averaging such that the dynamic schemes progressively switch from asymptotic schemes in the laminar regions towards DRP-like schemes in the turbulent regions. However, this requires some attention. First, it can be shown analytically, that a spatially varying discretization scheme is not symmetry-preserving [40,41] and therefore inevitably leads to a loss of conservation of kinetic energy. This was already observed in previous work [13], and the use of local averaging was therefore excluded in the present investigations. Secondly, it is not clear whether a local averaging approach would be advantageous at all. Indeed, since the dynamic coefficients respond to both the mean flow and the turbulent fluctuations, the dynamic coefficients in the laminar and turbulent regions might not differ much from each other. If so, global determination of the dynamic coefficient could be sufficient for accuracy improvement. This imple-

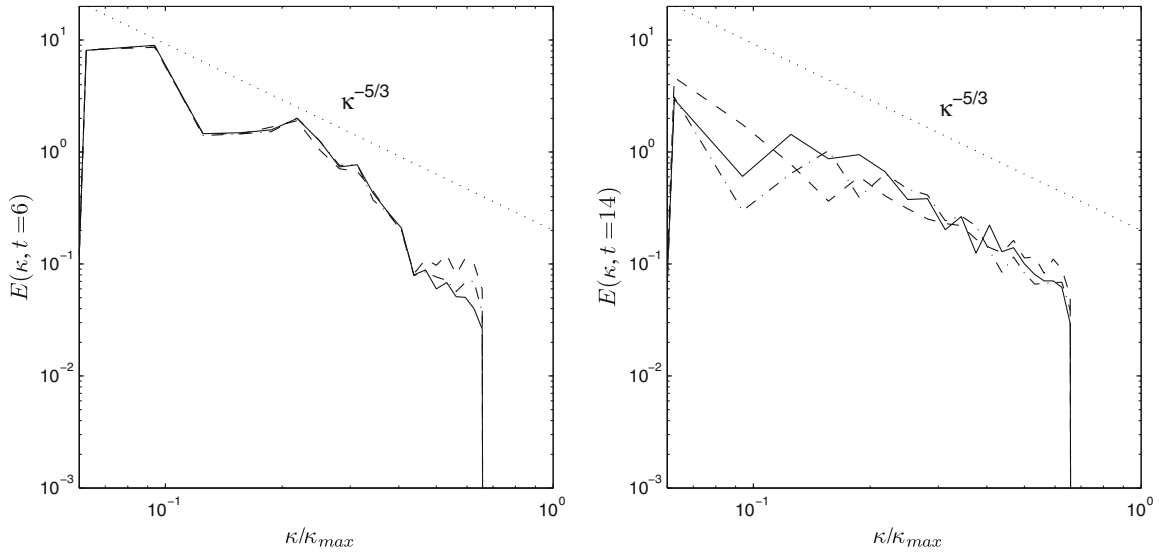

Fig. 19. Energy spectra of the filtered DNS (—), the pseudo-spectral LES (-·-·-) and the 2nd-order finite difference LES (– – –) in combination with the multiscale Smagorinsky model at times $t = 6$ (left) and $t = 14$ (right).

mentation would then be similar to that of Dispersion-Relation Preserving schemes, for which the stencil coefficients do not vary in space either. However, this issue certainly deserves further attention in future research.

Finally, the dynamic schemes are constructed and examined on uniform Cartesian meshes so far. Nevertheless, it is possible to extend the dynamic finite differencing technique to non-uniform Cartesian meshes by means of a coordinate transformation which maps the nonuniform grid onto a uniform grid. This approach, advocated by Vasilyev [42] and Verstappen and Veldman [40], allows to preserve the symmetry of the underlying derivative operators, leading to a symmetry-preserving discretization of the Navier–Stokes equations. The extension of the dynamic schemes to non-uniform Cartesian meshes will be investigated soon in future work.

9. Conclusions

In the present work, a general class of implicit *dynamic* finite difference schemes was developed which allow *numerically* accurate large-eddy simulations of turbulent flows. This new class of dynamic schemes forms a generalization of the explicit schemes that were already developed in earlier work of Fauconnier et al. [13]. Both implicit and explicit dynamic finite difference schemes allow to achieve optimal accuracy for all resolved scales of motion in the flow, rather than focusing only on the asymptotic order of accuracy for the largest resolved scales. This approach implies that the dynamic finite difference approximations minimize the total magnitude of the truncation error and thus preserve the global dispersion relation for all Fourier modes in the entire wavenumber range. The construction of the dynamic finite difference approximations relies on the determination of an optimal value for the coefficient in the leading order truncation term by combining the Taylor series expansions on two different grid resolutions. The method allows to extract a nearly optimal value, provided that a blending factor f is predefined, which allows comparison of the dynamic coefficient on both grids. This additional parameter was calibrated for $\mathrm{Re} \to \infty$, using a simplified inertial range spectrum. In this work, the numerical accuracy and the properties of the 2nd- and 4th-order explicit and a 4th-order implicit *dynamic* scheme were evaluated for the large-eddy simulation of the Taylor–Green vortex flow at $\mathrm{Re} = 1500$. Moreover, the interaction of these schemes with the dynamic Smagorinsky model and the multiscale Smagorinsky model were analyzed. The main conclusions on the quality of the developed dynamic finite difference schemes are enlisted below.

1. First it is concluded that the dynamic schemes systematically recover their potential asymptotic order of accuracy, regardless of the value of the blending factor f, provided that all scales of motion in the flow field are very well resolved on the computational grid. This asymptotic behaviour of the dynamic schemes is recovered in case the grid resolution is at least 8 times smaller then the smallest resolved scales in the laminar or turbulent flow field. Hence, the dynamic finite difference approximations adapt according to the smooth solution of the flow, focusing on maximum accuracy of the largest resolved scales. Obviously, this is an advantage over the Dispersion-Relation Preserving schemes which remain suboptimal in that case, since they are designed a priori for non-smooth solutions on the computational grid.
2. Once the resolution becomes inadequate to represent well all scales of motion in the laminar or turbulent flow, the dynamic schemes adjust the dynamic coefficient according to the spectral content of the solution on the computational grid. The Fourier characteristics of the dynamic finite difference approximation are adapted such that the global disper-

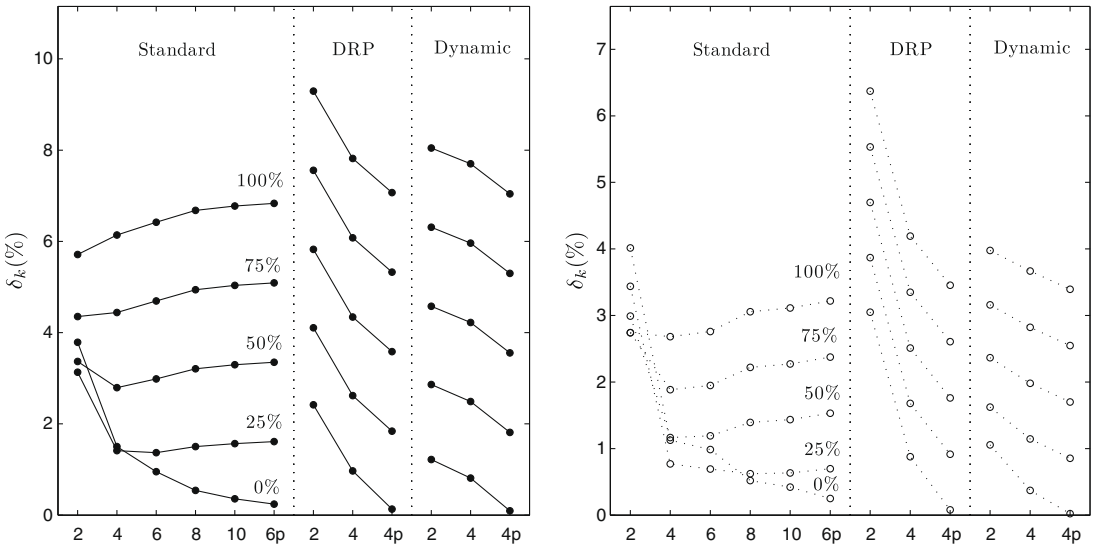

Fig. 20. Time-integrated total error norm at 100%, 75%, 50%, 25% and 0% of the modeling error. Dynamic Smagorinsky model (left) and multiscale Smagorinsky model (right).

sion error in the entire wavenumber range up to the filter cutoff is minimized. This corresponds to the minimization of the magnitude of the Taylor series that determines the entire truncation error.

3. As soon as the flow is fully turbulent and the energy spectrum exhibits an inertial range, both the dynamic finite difference schemes and the Dispersion-Relation Preserving schemes perform very similar. In general, the dynamic finite difference schemes tend to perform better due to their calibration with the correct slope of the energy spectrum for $\mathrm{Re} \to \infty$ and their ability to adapt to the resolution efficiency in each spatial direction of the computational mesh as well as the instantaneous flow characteristics.
4. The blending factor f is calibrated such that the dynamic scheme is optimal for a fully developed turbulent flow at $\mathrm{Re} \to \infty$. Since, the calibration was performed using an inertial range Kolmogorov spectrum, the optimal value for f it expected to be applicable for a wide range of turbulent flows. In this work, the sensitivity of the dynamic schemes to the value of the blending factor was investigated. It was observed that the sensitivity is quite small and that suboptimal values of f lead only to a small penalization.
5. Further, it was observed that the dynamic finite difference scheme is sensitive to the anisotropy of the resolved flow field in the large-eddy simulation of the Taylor–Green vortex. This could be a particularly interesting feature for the large-eddy simulation of more complex and anisotropic flows, or for grids with strongly different resolutions in each direction.
6. Finally, despite the substantial improvement in numerical accuracy obtained by the linear dynamic finite difference schemes and other high-order schemes, these schemes do not necessarily provide a more accurate solution of the large-eddy simulation. Indeed, in comparison with more accurate numerical schemes, less accurate methods can lead to advantageous cancellation between numerical errors and modeling errors, resulting into a reduction of the total errors. These observations confirm the results in [16,32,1]. However, it was also demonstrated that the development of new and better subgrid models necessitates the use of more accurate methods in order to obtain minimal total errors. Although it is tempting to resign to application of lower order discretizations in combination with dissipative models, trusting upon contingent cancellation of errors, the present work rather advocates to develop better models in combination with highly-accurate discretizations such that both numerical errors and modeling errors are controlled more systematically.

The former conclusions confirm that the developed family of dynamic finite difference approximations can be a useful and viable tool for numerically accurate large-eddy simulations of turbulent flows. Since the dynamic schemes do not require any limitation of the dynamic coefficients in order to assure stability, we are confident that the method can be used as a black box in more complex applications in combination with an appropriate choice of the blending factor f. As discussed in Section 4.2 one may justify the use of an additional clipping on the dynamic coefficients in practical simulations with no de-aliasing in order to control the optimization interval of the dynamic schemes. The current implementation of the dynamic schemes required only a computational overhead of 1.7%, which is negligible in comparison with the gain in accuracy.

Acknowledgment

This research was funded by a Ph.D. grant of the Institute for the Promotion of Innovation through Science and Technology in Flanders (IWT-Vlaanderen).

Appendix A. Three dynamic finite difference approximations

Here, a selection of three dynamic finite difference approximations are described, i.e. the 2nd- and 4th-order explicit dynamic finite difference approximations and the 4th-order implicit dynamic finite difference approximation. The coarse resolution is chosen twice the fine resolution such that $\alpha = 2$.

A.1. Second-order explicit dynamic finite difference approximation

The basic expression for both the 2nd-order dynamic finite difference approximations of the first derivative in a node $\bar{u}(x_i) = \bar{u}_i$ reads

$$\overline{\frac{\partial u}{\partial x}}(x) = \frac{\delta \bar{u}}{\delta x} + c_{2,1}^{dyn} \Delta^2 \frac{\delta^3 \bar{u}}{\delta x^3}, \quad c_{2,1}^{dyn} = c_{2,1}^{*} \frac{\left\langle \left(\frac{\delta^3 \bar{u}}{\delta x^3}\right)^2 - 4 f c_{2,3}^{*} \Delta^2 \left(\frac{\delta^5 \bar{u}}{\delta x^5}\right)\left(\frac{\delta^3 \bar{u}}{\delta x^3}\right) \right\rangle}{\left\langle \left(\frac{\delta^3 \bar{u}}{\delta x^3} - 4 f c_{2,3}^{*} \Delta^2 \frac{\delta^5 \bar{u}}{\delta x^5}\right)^2 \right\rangle}, \tag{86}$$

whereas the expression for the second derivative in $\bar{u}(x_i) = \bar{u}_i$ yields

$$\overline{\frac{\partial^2 u}{\partial x^2}}(x) = \frac{\delta^2 \bar{u}}{\delta x^2} + c_{2,2}^{dyn} \Delta^2 \frac{\delta^4 \bar{u}}{\delta x^4}, \quad c_{2,2}^{dyn} = c_{2,2}^{*} \frac{\left\langle \left(\frac{\delta^4 \bar{u}}{\delta x^4}\right)^2 - 4 f c_{2,4}^{*} \Delta^2 \left(\frac{\delta^6 \bar{u}}{\delta x^6}\right)\left(\frac{\delta^4 \bar{u}}{\delta x^4}\right) \right\rangle}{\left\langle \left(\frac{\delta^4 \bar{u}}{\delta x^4} - 4 f c_{2,4}^{*} \Delta^2 \frac{\delta^6 \bar{u}}{\delta x^6}\right)^2 \right\rangle}. \tag{87}$$

From Taylor expansion the values $c_{2,1}^{*} = -\frac{1}{6}$ and $c_{2,3}^{*} = -\frac{1}{4}$ are obtained for the first derivative, whereas $c_{2,2}^{*} = -\frac{1}{12}$ and $c_{2,4}^{*} = -\frac{1}{6}$ are obtained for the second derivative. The discretization stencil for these basic schemes as well as for the derivatives in the calculation of the dynamic coefficients are given in Table 2.

A.2. Fourth-order explicit dynamic finite difference approximation

The basic expression for the dynamic finite difference approximation of the first derivative in a node $\bar{u}(x_i) = \bar{u}_i$ reads

$$\overline{\frac{\partial u}{\partial x}}(x) = \frac{\delta \bar{u}}{\delta x} + c_{4,1}^{dyn} \Delta^4 \frac{\delta^5 \bar{u}}{\delta x^5}, \quad c_{4,1}^{dyn} = c_{4,1}^{*} \frac{\left\langle \left(\frac{\delta^5 \bar{u}}{\delta x^5}\right)^2 - \frac{16}{5} f c_{2,5}^{*} \Delta^2 \left(\frac{\delta^7 \bar{u}}{\delta x^7}\right)\left(\frac{\delta^5 \bar{u}}{\delta x^5}\right) \right\rangle}{\left\langle \left(\frac{\delta^5 \bar{u}}{\delta x^5} - \frac{16}{5} f c_{2,5}^{*} \Delta^2 \frac{\delta^7 \bar{u}}{\delta x^7}\right)^2 \right\rangle}, \tag{88}$$

whereas the expression for the second derivative in $\bar{u}(x_i) = \bar{u}_i$ yields

$$\overline{\frac{\partial^2 u}{\partial x^2}}(x) = \frac{\delta^2 \bar{u}}{\delta x^2} + c_{4,2}^{dyn} \Delta^4 \frac{\delta^6 \bar{u}}{\delta x^6}, \quad c_{4,2}^{dyn} = c_{4,2}^{*} \frac{\left\langle \left(\frac{\delta^6 \bar{u}}{\delta x^6}\right)^2 - \frac{16}{5} f c_{2,6}^{*} \Delta^2 \left(\frac{\delta^8 \bar{u}}{\delta x^8}\right)\left(\frac{\delta^6 \bar{u}}{\delta x^6}\right) \right\rangle}{\left\langle \left(\frac{\delta^6 \bar{u}}{\delta x^6} - \frac{16}{5} f c_{2,6}^{*} \Delta^2 \frac{\delta^8 \bar{u}}{\delta x^8}\right)^2 \right\rangle}. \tag{89}$$

From Taylor expansion the values $c_{4,1}^{*} = \frac{1}{30}$ and $c_{2,5}^{*} = -\frac{1}{3}$ are obtained for the first derivative, while $c_{4,2}^{*} = \frac{1}{90}$ and $c_{2,6}^{*} = -\frac{1}{4}$ are obtained for the second derivative. The discretization stencil for the basic scheme as well as for the derivatives in the calculation of the dynamic coefficient are given in Table 2

A.3. Fourth-order implicit dynamic finite difference approximation

The basic expression for the 4th-order dynamic implicit finite difference approximation of the first derivative in a node $\bar{u}(x_i) = \bar{u}_i$ can be formulated as

$$\sum_{l=-1}^{1} \alpha_l \left(\frac{c_{4,1}^{dyn}}{c_{4,1}^{*}}\right) \overline{\frac{\partial u}{\partial x}}(x_{i+l}) = \sum_{j=-2}^{2} \frac{\beta_j}{\Delta} \left(\frac{c_{4,1}^{dyn}}{c_{4,1}^{*}}\right) \bar{u}(x_{i+j}), \tag{90}$$

in which $c_{4,1}^{dyn}$ is calculated with expression (26), leading to

$$c_{4,1}^{dyn} = c_{4,1}^{*} \frac{\left\langle \left(\frac{\delta^5 \bar{u}}{\delta x^5}\right)^2 - \frac{16}{5} f c_{2,5}^{*} \Delta^2 \left(\frac{\delta^7 \bar{u}}{\delta x^7}\right)\left(\frac{\delta^5 \bar{u}}{\delta x^5}\right) \right\rangle}{\left\langle \left(\frac{\delta^5 \bar{u}}{\delta x^5} - \frac{16}{5} f c_{2,5}^{*} \Delta^2 \frac{\delta^7 \bar{u}}{\delta x^7}\right)^2 \right\rangle}. \tag{91}$$

From Taylor expansion the values $c_{4,1}^{*} = -\frac{1}{120}$ and $c_{2,5}^{*} = -\frac{1}{3}$ are obtained. The basic expression for the 4th-order dynamic implicit finite difference approximation of the second derivative in a node $\bar{u}(x_i) = \bar{u}_i$ can be formulated as

Table 2
Overview of the stencils of the three selected dynamic finite difference approximation. Note that $\beta_i = -\beta_{-i}$ for the odd derivatives whereas $\beta_i = \beta_{-i}$ for the even derivatives.

n	α_0	$\alpha_{\pm1}$	β_0	$\pm\beta_{\pm1}$	$\pm\beta_{\pm2}$	$\pm\beta_{\pm3}$	$\pm\beta_{\pm4}$	$\mathcal{O}(\Delta^k)$
1			0	$-c_{2,1}^{dyn}+\frac{1}{2}$	$\frac{1}{2}c_{2,1}^{dyn}$			2
1			0	$\frac{2}{3}+\frac{5}{2}c_{4,1}^{dyn}$	$-\frac{1}{12}-2c_{4,1}^{dyn}$	$\frac{1}{2}c_{4,1}^{dyn}$		4
1	1	$\frac{1}{4}+\frac{1}{12}\frac{c_{4,1}^{dyn}}{c_{4,1}^{*}}$	0	$\frac{3}{4}+\frac{1}{36}\frac{c_{4,1}^{dyn}}{c_{4,1}^{*}}$	$\frac{1}{36}\frac{c_{4,1}^{dyn}}{c_{4,1}^{*}}$			4
2			$6c_{2,2}^{dyn}-2$	$1-4c_{2,2}^{dyn}$	$c_{2,2}^{dyn}$			2
2			$-\frac{5}{2}-20c_{4,2}^{dyn}$	$\frac{4}{3}+15c_{4,2}^{dyn}$	$-6c_{4,2}^{dyn}-\frac{1}{12}$	$c_{4,2}^{dyn}$		4
2	1	$\frac{1}{10}+\frac{9}{110}\frac{c_{4,2}^{dyn}}{c_{4,2}^{*}}$	$-\frac{12}{5}+\frac{9}{110}\frac{c_{4,2}^{dyn}}{c_{4,2}^{*}}$	$\frac{6}{5}-\frac{6}{55}\frac{c_{4,2}^{dyn}}{c_{4,2}^{*}}$	$\frac{3}{44}\frac{c_{4,2}^{dyn}}{c_{4,2}^{*}}$			4
3			0	-1	$\frac{1}{2}$			2
4			6	-4	1			2
5			0	$\frac{5}{2}$	-2	$\frac{1}{2}$		2
6			-20	15	-6	1		2
7			0	-7	7	-3	$\frac{1}{2}$	2
8			70	-56	28	-8	1	2

$$\sum_{l=-1}^{1}\alpha_l\left(\frac{c_{4,2}^{dyn}}{c_{4,2}^{*}}\right)\overline{\frac{\partial^2 u}{\partial x^2}}(x_{i+l})=\sum_{j=-2}^{2}\frac{\beta_j}{\Delta^2}\left(\frac{c_{4,2}^{dyn}}{c_{4,2}^{*}}\right)\bar{u}(x_{i+j}), \tag{92}$$

in which $c_{4,2}^{dyn}$ is calculated with expression (26), leading to

$$c_{4,2}^{dyn}=c_{4,2}^{*}\frac{\left\langle\left(\frac{\delta^6\bar{u}}{\delta x^6}\right)^2-\frac{16}{5}fc_{2,6}^{*}\Delta^2\left(\frac{\delta^8\bar{u}}{\delta x^8}\right)\left(\frac{\delta^6\bar{u}}{\delta x^6}\right)\right\rangle}{\left\langle\left(\frac{\delta^6\bar{u}}{\delta x^6}-\frac{16}{5}fc_{2,6}^{*}\Delta^2\frac{\delta^8\bar{u}}{\delta x^8}\right)^2\right\rangle}. \tag{93}$$

From Taylor expansion the values $c_{4,2}^{*}=-\frac{1}{200}$ and $c_{2,6}^{*}=-\frac{1}{4}$ are obtained. The discretization stencil for the basic scheme as well as for the derivatives in the calculation of the dynamic coefficient are given in Table 2.

Although the higher derivatives in the former expressions can be obtained by implicit finite difference approximations, no attempt is done in this work. Hence, these derivatives are calculated using standard explicit finite difference approximations.

References

[1] J. Meyers, B. Geurts, M. Baelmans, Optimality of the dynamic procedure for large-eddy simulations, Phys. Fluids 17 (4) (2005) 045–108.
[2] S. Ghosal, An analysis of numerical errors in large-eddy simulations of turbulence, J. Comput. Phys. 125 (January) (1996) 187–206.
[3] A.G. Kravchenko, P. Moin, On the effect of numerical errors in large-eddy simulations of turbulent flows, J. Comput. Phys. 131 (September) (1997) 310–322.
[4] F.K. Chow, P. Moin, A further study of numerical errors in large-eddy simulations, J. Comput. Phys. 184 (September) (2003) 366–380.
[5] J. Berland, C. Bogey, C. Bailly, A study of differentiation errors in large-eddy simulations based on the EDQNM theory, J. Comput. Phys. 227 (2008) 8314–8340.
[6] S.A. Orszag, On the elimination of aliasing in finite-difference schemes by filtering high-wavenumber components, J. Atmos. Sci. 28 (April) (1971) 1074.
[7] N. Park, K. Mahesh, Analysis of numerical errors in large eddy simulation using statistical closure theory, J. Comput. Phys. 222 (March) (2007) 194–216.
[8] C.K.W. Tam, J.C. Webb, Dispersion-relation-preserving finite difference schemes for computational acoustics, J. Comput. Phys. 107 (1993) 262–281.
[9] J.W. Kim, D.T. Lee, Optimized compact finite difference schemes with maximum resolution, AIAA J. 34 (5) (1996) 887–893.
[10] R. Hixon, Nonlinear comparison of high-order and optimized finite-difference schemes, Int. J. Comput. Fluid Dynam. 13 (3) (2000) 259–277.
[11] G. Ashcroft, X. Zhang, Optimized prefactored compact schemes, J. Comput. Phys. 190 (2003) 459–477.
[12] C. Bogey, C. Bailly, A family of low dispersive and low dissipative explicit schemes for flow and noise computations, J. Comput. Phys. 194 (2004) 194–214.
[13] D. Fauconnier, C.De Langhe, E. Dick, A family of dynamic finite difference schemes for large-eddy simulation, J. Comput. Phys. 228 (6) (2009) 1830–1861.
[14] M.E. Brachet, D.I. Meiron, S.A. Orszag, B.G. Nickel, R.H. Morf, U. Frisch, Small-scale structure of the Taylor–Green vortex, J. Fluid. Mech. 130 (1983) 411–452.
[15] B. Vreman, B. Geurts, H. Kuerten, Comparison of numerical schemes in large-eddy simulations of the temporal mixing layer, Int. J. Numer. Methods Fluids 22 (1996) 297–311.
[16] J. Meyers, B. Geurts, M. Baelmans, Database analysis of errors in large-eddy simulation, Phys. Fluids 15 (9) (2003) 2740–2755.
[17] S.K. Lele, Compact finite difference schemes with spectral-like resolution, J. Comput. Phys. 103 (1991) 16–42.
[18] T. Gotoh, D. Fukayama, Pressure spectrum in homogeneous turbulence, Phys. Rev. Lett. 86 (17) (2001) 3775–3778.
[19] G.I. Taylor, A.E. Green, Mechanism of the production of small eddies from large ones, Roy. Soc. London Proc. Series A 158 (February) (1937) 499–521.
[20] S.A. Orszag, Numerical simulation of the Taylor–Green vortex, in: Proceedings of the International Symposium on Computing Methods in Applied Sciences and Engineering, Part 2, Springer-Verlag, London, UK, 1974, pp. 50–64.
[21] T.S. Lund, H.J. Kaltenbach, Experiments with explicit filtering for les using a finite-difference method, Annual research briefs Center for Turbulence Research, Stanford, 1995.
[22] T.S. Lund, On the use of discrete filters for large eddy simulation. Annual research briefs, Center for Turbulence Research, Stanford, 1997.
[23] J. Gullbrand, F.K. Chow, Investigations of numerical errors, subfilter-scale models, and subgrid-scale models in turbulent channel flow simulatons, in: P. Bradshaw (Ed.), Proceedings of the Summer Program 2002, Stanford University and Nasa Ames Research Center, Stanford, 2002, pp. 87–104.

[24] J. Gullbrand, F.K. Chow, The effect of numerical errors and turbulence models in large eddy simulations of channel flow with and without explicit filtering, J. Fluid. Mech. 495 (2003) 323–341.
[25] T. Brandt, A priori tests on numerical errors in large eddy simulation using finite differences and explicit filtering, Int. J. Numer. Methods Fluids 51 (June) (2006) 635–657.
[26] T. Brandt, Study on numerical and modelling errors in LES using a priori and a posteriori, Ph.D. Dissertation, Helsinki University of Technology, Deptartment of Mechanical engineering, P.O. Box 4400, FI-02015 TKK, 2007. ISBN 978-951-22-8634-8.
[27] J. Berland, C. Bogey, O. Marsden, C. Bailly, High-order low dispersive and low dissipative explicit schemes for multiple-scale and boundary problems, J. Comput. Phys. 224 (2007) 637–662.
[28] M. Germano, U. Piomelli, P. Moin, W.H. Cabot, A dynamic subgrid-scale eddy viscosity, Phys. Fluids A 3 (7) (1991) 1760–1765.
[29] D.K. Lilly, The representation of small-scale turbulence in numerical simulation experiments, in: Proceedings of IBM Scientific Computing Symposium on Environmental Sciences, IBM Data Processing Division, Goldstine H.H., Yorktown Heights, New York, 1967, pp. 159–210.
[30] T.J.R. Hughes, L. Mazzei, A.A. Oberai, A.A. Wray, The multiscale formulation of large eddy simulation: decay of homogeneous isotropic turbulence, Phys. Fluids 13 (2) (2001) 505–512.
[31] T.J.R. Hughes, A.A. Oberai, L. Mazzei, Large eddy simulation of turbulent channel flows by the variational multiscale method, Phys. Fluids 13 (6) (2001) 1784–1799.
[32] J. Meyers, Accuracy of large-eddy simulation strategies, Ph.D. Dissertation, KUL, Faculteit toegepaste wetenschappen, Departement werktuigkunde, Toegepaste mechanica en energieconversie, Leuven, 2004. ISBN 90-5682-473-2.
[33] J. Meyers, B. Geurts, P. Sagaut, A computational error-assessment of central finite-volume discretizations in large-eddy simulation using a Smagorinsky model, J. Comput. Phys. 227 (2007) 156–173.
[34] S. Hickel, N.A. Adams, J.A. Domaradzki, An adaptive local deconvolution method for implicit les, J. Comput. Phys. 213 (1) (2006) 413–436.
[35] S.B. Pope, Turbulent Flows, Cambridge University Press, Cambridge, 2000.
[36] S. Stolz, N.A. Adams, L. Kleiser, An approximate deconvolution model for large-eddy simulation with application to incompressible wall-bounded flows, Phys. Fluids 13 (April) (2001) 997–1015.
[37] J.A. Domaradzki, N.A. Adams, Direct modelling of subgrid scales of turbulence in large eddy simulations, J. Turbul. 3 (April) (2002). 24–+.
[38] D. Fauconnier, C. De Langhe, E. Dick, The dynamic procedure for accuracy improvement of numerical discretizations in fluid mechanics, J. Comput. Phys. 224 (2007) 1095–1123.
[39] D. Fauconnier, C. De Langhe, E. Dick, The sampling-based dynamic procedure as tool for higher-order discretization, Int. J. Numer. Methods Fluids 56 (2008) 1241–1247.
[40] R.W.C.P. Verstappen, A.E.P. Veldman, Symmetry-preserving discretization of turbulent flow, J. Comput. Phys. 187 (2003) 343–368.
[41] J.G. Wissink, On unconditional conservation of kinetic energy by finite-difference discretizations of the linear and non-linear convection equation, Comput. Fluids 33 (2) (2004) 315–343.
[42] O.V. Vasilyev, High order finite difference schemes on non-uniform meshes with good conservation properties, J. Comput. Phys. 157 (January) (2000) 746–761.